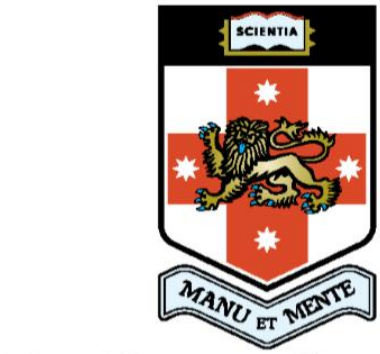

UNSW
SYDNEY

Ag-Incorporated Lead Halide Perovskite Single Crystal for Tunable Bandgap and Mobility Enhancement

A thesis submitted in complete fulfilment of the

requirements for the award of the degree of

Master of Science

by

Tengyue He

School of Materials Science and Engineering

Faculty of Science

University of New South Wales

May 2020

Thesis dissertation sheet

Surname/Family Name	:	**He**
Given Name/s	:	**Tengyue**
Abbreviation for degree as give in the University calendar	:	**MSC**
Faculty	:	**Faculty of Science**
School	:	**School of Materials Science and Engineering**
Thesis Title	:	**Ag-Incorporated Lead Halide Perovskite Single Crystal for Tunable Bandgap and Mobility Enhancement**

Abstract 350 words maximum: (PLEASE TYPE)

Intrinsic metal halide perovskite single crystal has attracted intensive attention in recent years due to its excellent optoelectronic properties. Also, controlled doping of metal halide perovskite with metal ions is a feasible way to adjust its optoelectronic properties. However, only a few metal ions (Bi^{3+}, Fe^{3+}, Sn^{2+}) doping of lead halide perovskite single crystal works were reported. Here, we employed a low-temperature high-molarity crystallization (LTHMC) method to synthesize high-quality monovalent Ag ions doped $CH_3NH_3PbBr_3$ single crystals. Ag^+ incorporation leads a 160 meV reduction on the bandgap of Ag-doped single crystals, while significant PL quenching was observed. P-type behaviour of Ag-doped $CH_3NH_3PbBr_3$ single crystals and enhancement on conductivity and carrier concentration were confirmed by Hall effect measurement. Space-charge limited current methods was adopted to obtain the mobility of various doping levels samples. Compared with pristine single crystal, the mobility of Ag-doped single crystal exhibits a near sixfold enhancement. Moreover, photodetector based on Ag-doped single crystal was fabricated, exhibiting better performance than undoped counterpart. This project manifests the successful introduction of silver ions in perovskite crystals while retaining the host lattice structure, presenting an effective path for adjusting the optoelectronic properties of perovskites.

ORIGINALITY STATEMENT

'I hereby declare that this submission is my own work and to the best of my knowledge it contains no materials previously published or written by another person, or substantial proportions of material which have been accepted for the award of any other degree or diploma at UNSW or any other educational institution, except where due acknowledgement is made in the thesis. Any contribution made to the research by others, with whom I have worked at UNSW or elsewhere, is explicitly acknowledged in the thesis. I also declare that the intellectual content of this thesis is the product of my own work, except to the extent that assistance from others in the project's design and conception or in style, presentation and linguistic expression is acknowledged.'

Signed …….....

Date …….…….

INCLUSION OF PUBLICATIONS STATEMENT

UNSW is supportive of candidates publishing their research results during their candidature as detailed in the UNSW Thesis Examination Procedure.

Publications can be used in their thesis in lieu of a Chapter if:

- The candidate contributed greater than 50% of the content in the publication and is the "primary author", ie. the candidate was responsible primarily for the planning, execution and preparation of the work for publication
- The candidate has approval to include the publication in their thesis in lieu of a Chapter from their supervisor and Postgraduate Coordinator.
- The publication is not subject to any obligations or contractual agreements with a third party that would constrain its inclusion in the thesis

Please indicate whether this thesis contains published material or not:

☒ This thesis contains no publications, either published or submitted for publication
(if this box is checked, you may delete all the material on page 2)

☐ Some of the work described in this thesis has been published and it has been documented in the relevant Chapters with acknowledgement
(if this box is checked, you may delete all the material on page 2)

☐ This thesis has publications (either published or submitted for publication) incorporated into it in lieu of a chapter and the details are presented below

CANDIDATE'S DECLARATION

I declare that:

- I have complied with the UNSW Thesis Examination Procedure
- where I have used a publication in lieu of a Chapter, the listed publication(s) below meet(s) the requirements to be included in the thesis.

Candidate's Name	**Signature**	**Date (dd/mm/yy)**
Tengyue He		

COPYRIGHT STATEMENT

Signed …….....

Date …….....

AUTHENTICITY STATEMENT

‘I certify that the Library deposit digital copy is a direct equivalent of the final officially approved version of my thesis.’

Signed …….....

Date …….....

Acknowledgment

Two years of study as a master student has come to an end before I know it, a bittersweet moment especially reinforced by the pandemic. In this journey, I am honored to have enjoyed the company of respectable teachers and faculties who have witnessed my growth and guided me along the way. I am also grateful for my fellow group members who have studied closely with me. It has been fun and fulfilling.

First and foremost, I would love to express my sincere gratitude to my supervisor, Professor Tom Wu, for providing me an opportunity to be involved in this incredible opportunity to work on this fabulous and intriguing project as a master by research. During the past two years, Prof. Tom Wu has offered me a great amount of help, not only in scientific research projects, but also when it comes to other aspects of my overall ability. He attaches great importance to training students' abilities. In scientific research, he would share his opinions and suggestions with us in a timely and respectful manner. In the weekly group meetings, he would go great length to communicate with me in detail to ensure that our plan goes smoothly. He always tells us to not hesitate to contact him if we meet any problems. Moreover, he would make frequent visits to the laboratory to inquire on our progress and to offer much needed guidance. As a laboratory manager, he has always been responsible and led by example, such as organizing the laboratory in an orderly manner and cleaning up the experimental garbage. I am deeply motivated and inspired by his work ethic.

Furthermore, I want to thank the postdocs in our group, Dr. Chun-Ho Lin and Dr. Long Hu, who helped me finish the measurements and analyze experimental data. I would also like to extend my gratitude to my kind and selfless fellow group members. When we encountered difficulties, we would always support each other to come out better researchers and humans.

Last but not least, to my parents and my girlfriend, I cannot thank you enough for the continuous encouragement in both my personal life and career as a postgraduate.

Abstract

Intrinsic metal halide perovskite single crystal has attracted intensive attention in recent years due to its excellent optoelectronic properties. Also, controlled doping of metal halide perovskite with metal ions is a feasible way to adjust its optoelectronic properties. However, only a few metal ions (Bi^{3+}, Fe^{3+}, Sn^{2+}) doping of lead halide perovskite single crystal works were reported. Here, we employed a low-temperature high-molarity crystallization (LTHMC) method to synthesize high-quality monovalent Ag ions doped $CH_3NH_3PbBr_3$ single crystals. Ag^+ incorporation leads a 160 meV reduction on the bandgap of Ag-doped single crystals, while significant PL quenching was observed. P-type behavior of Ag-doped $CH_3NH_3PbBr_3$ single crystals and enhancement on conductivity and carrier concentration were confirmed by Hall effect measurement. Space-charge limited current methods was adopted to obtain the mobility of various doping levels samples. Compared with pristine single crystal, the mobility of Ag-doped single crystal exhibits a near six fold enhancement. Moreover, photodetector based on Ag-doped single crystal was fabricated, exhibiting better performance than undoped counterpart. This project manifests the successful introduction of silver ions in perovskite crystals while retaining the host lattice structure, presenting an effective path for adjusting the optoelectronic properties of perovskites.

Table of Contents

LIST OF ABBREVIATIONS

MA^+	$CH_3NH_3^+$	**FA^+**	$CH(NH_2)_2^+$
HOIP	hybrid organic-inorganic perovskite	**LEDs**	light-emitting didoes
FETs	field-effect transistors	**HTL**	hole transport layer
ETL	electron transport layer	**PCE**	power conversion efficiency
NCs	Nanocrystals	**UPS**	ultraviolet photoelectron spectroscopy
PSCs	perovskite solar cells	**NIR**	near infrared region
LHP	lead halide perovskite	**PLQYs**	photoluminescence quantum yields
PLE	PL excitation	**FF**	Fill factor
TRMC	time-resolved microwave conductivity	**VB**	Valence Band
CB	Conduction Band	**NPs**	nanoparticles
TRPL	Time-resolved photoluminescence	**WLED**	white-light-emitting diodes
NTSC	National Television System Committee	**STL**	Solution temperature lowering
BSSG	bottom seeded solution growth	**TSSG**	top seeded solution growth
ITC	inverse temperature crystallization	**GBL**	γ-butyrolactone
DMF	N, N-dimethylformamide	**DMSO**	dimethylsulphoxide
LTGC	low-temperature-gradient crystallization	**AVC**	antisolvent vapor-assisted crystallization
DCM	Dichloromethane	**LTHMC**	low temperature high molarity crystallization
XRD	X-ray Diffraction	**XPS**	X-ray Photoelectron Spectroscopy
PL	Photoluminescence	**SCLC**	Space-Charge-Limited-Current
TFL	Trap-filled limited	**PPMS**	Physical property measurement system
E_A	activation energy		

LIST OF ILLUSTRATIONS

Chapter 1 – Introduction

The term "perovskite" originated from Russian scientist Lev Perovski, and it was first used for $CaTiO_3$ which reported by Gustav in 1839.[1,2] Inorganic hybrid perovskite was first reported in 1958 by Moller with an ABX_3 structure where A-site cation is cesium ions, B-site cation is lead ions and X-site are halogen elements (i.e. Cl, Br, I).[3] Author discovered that the photoconductivity could be altered by changing the halogen elements in X site to attain diverse spectral responses range. Halide perovskite with big organic cation, methylammonium (MA^+) was reported in 1978 by Weber.[4] Since then, as a new type of semiconductor material system, hybrid organic-inorganic perovskite (HOIP) has brought a new revolution in the field of optoelectronic applications, such as solar cell[5-7], lasers[8-11], light-emitting didoes[12-14] (LEDs), photodetector in different range[15-18], field-effect transistors[19-22] (FETs), resistive switching memories devices[23-26], etc. The unique attributes of HOIP are high absorption coefficient, tunable direct bandgap, long carrier diffusion length, low trap-state density and high charge carrier (electron/hole) mobility.[27-31] Among the field of optoelectronic applications based on perovskite material, solar cell attracts the most intensive attention from scientists and research groups. In the past decade, perovskite solar cell was investigated thoroughly in various parts, such as device configurations, interface engineering[6], hole/electron transport layer[32,33] (HTL, ETL), stability[34-36], etc. With the improvement of various sections of perovskite solar cell, the power conversion efficiency (PCE), which is the most crucial parameter for evaluating performance of solar cell, has been increased from 3.9%[37] to nearly 25.2%[38] in the past ten years. Consequently, HOIP has already achieved huge success in the field of

optoelectronic devices and the revolution led by it is still in full swing.

Chapter 2 – Literature Review of Metal Doped Lead Halide Perovskites

2.1 Introduction of Hybrid Organic-Inorganic Lead Halide Perovskites

Hybrid organic-inorganic lead halide perovskite as a large clan of material system adopts the same three-dimensional chemical formula ABX_3, A site is occupied by large organic or inorganic cation, wherein the B site is a divalent cation with smaller ionic diameter than A site and X-site is filled with three halogen anions.[39] The cation located at A site is generally classified into organic cation and inorganic cation, the organic cations are normally MA^+ ($CH_3NH_3^+$) and FA^+($CH(NH_2)_2^+$), and the inorganic cations are mostly Cs^+. The divalent metal cations at the B site are generally Pb^{2+}, Sn^{2+}.[40] The ions at different positions are not limited to one type and it could be a mixture of various types as well. In an independent unit cell, the ionic radius of the cation located at A site is the largest at three positions, which each 1/8 of the cation are distributed at the eight corners of the unit cell. Three monovalent halogen ions are distributed in the middle of six faces. The only complete ion in the unit cell is the B-site small cation, which is located at the center of the cube. Octahedral structure of BX_6 formed by B cations which assemble X anions around, assembling a 3D structure attached at the corners, as shown in **Figure 1**[28]. To investigate the stability of the perovskite compound with the ABX_3 structure, Goldschmidt reported the concept of tolerance factor (t) in 1927, which is defined as:

$$t = \frac{R_A + R_B}{\sqrt{2}(R_B + R_x)} \quad (1)$$

where R_A, R_B and R_X are the ionic radius of the two cations(A B) and X-site halogen anions, respectively.[41] According to experimental results and calculation simulation, the appropriate range of tolerance factor is 0.8~1, on which perovskite structure can be formed. For example, when t is smaller than 0.8, $Cs_xFA_{1-x}PbI_3$ is δ phase without photoactivity instead of the black α phase. Stability of perovskite solar cell can be influenced by the tolerance factor significantly, which the value is specified between 0.94-0.98.[42]

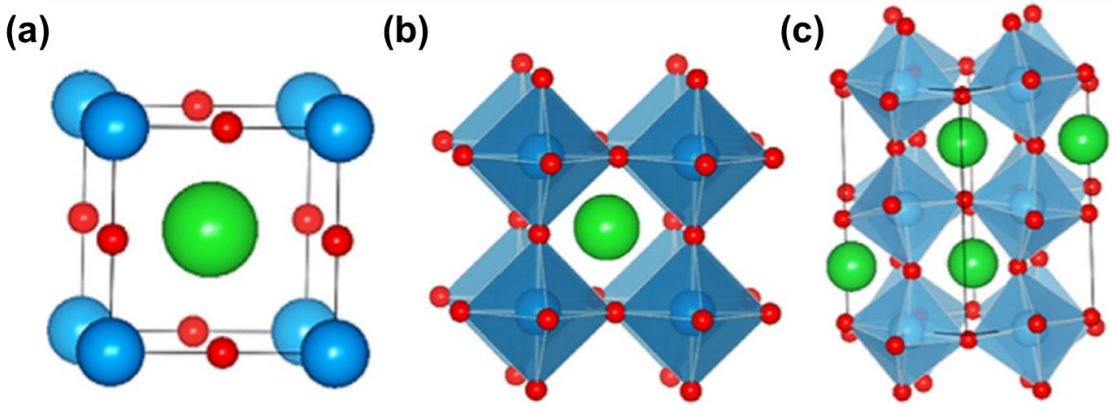

Figure 1. Cubic perovskite unit cell. (a) A site cation locates in the eight corners of cubic, B site cation occupies the center of the cubic, and X site anions are in the lattice faces. (b) A different view to illustrate BX_6 octahedra. (c) Tilted BX_6 octahedra caused by inappropriate cations/anions sizes or another factor.[28]

In the past decade, enormous publications have reported various doping effects in three sites in ABX_3 to elevate the achievements of HOIPs optoelectronic application in terms of stability, optical property, and electrical property, etc.[43-46] In this thesis, B site doping will be the main idea to adjust the unique properties of HOIPs single crystal. B site doping works will be introduced in the next part.

2.2 B-site Metal Doped Lead Halide Perovskites

Lead cation is the most common B site cation in HOIPs, and its superior virtues of stability and charge transport compared with Sn base have been proved already. However, optoelectronic properties of perovskites are determined by B-X bonds in each unit cell, so that optoelectronic properties could be altered through replaced or partially substituting by other metal elements in B site. (i.e. Sn^{2+}, Ge^{2+}) Moreover, lead, a highly toxic element, is considered a threat to human health and the environment, and B site dope could mitigate the hazards of lead based perovskites. To realize the best possible of B site doping effects, doping work review will be divided into three parts, which are monovalent, divalent and heterovalent.

2.2.1 B-site Monovalent Ions Doped Lead Halide Perovskites

The works of B site doped by monovalent ions are less studied compared to that of other valence ions because monovalent ions are more appropriate for A-site dope, such as Cs^{+}, Rb^{+}, K^{+}.[47-49] In this part, I will introduce two excellent doping works of Ag^{+} doped lead halide perovskite thin films and Nanocrystals (NCs).

In 2017, Chen et al. fabricated a planer heterojunction solar cells based on Ag-incorporated $MAPbI_3$ and $MAPbI_xCl_{3-x}$ thin films.[50] AgI was added into pure $MAPbI_3$ precursor to synthesize $MAPb_xAg_{1-x}I_3$ thin films by spin coating. As shown in **Figure 2**, film morphology and crystallinity were enhanced after doping with Ag^{+}, and fermi level was shifted as well.

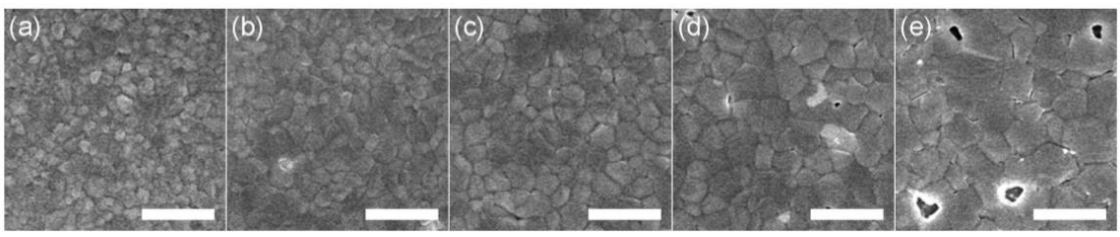

Figure 2. SEM graphs of Ag-doped $MAPbI_3$ films with different doping concentration (a) 0%, (b) 0.5%, (c) 1.0%, (d) 2.5%, (e) 5.0%. Scale bar is 1.0 micrometer.[50]

Fermi level drops down to the middle of bandgap from near conduction band, suggesting that perovskite is changing from n-type semiconductor to intrinsic semiconductor behavior by incorporating with silver. Moreover, achievements of the solar cell adopted Ag-doped $MAPbI_3$ thin films have reached a new level, in which the PCE is increased from 16% to 18.4% after doping with 0.5% Ag ions. **Table 1** shows the Performance of Solar cell change with Ag doping concentration. This work demonstrated that monovalent ions could be used for adjusting properties of HOIP and enhance the performance of HOIP's applications.

Table 1. Performance of Ag-Incorporated $MAPbI_3$ Solar Cell

Ag (%)	V (V)	J (mA cm^{-2})	Fill Factor	PCE (%)
0	1.09	19.3	0.76	16.0(14.7±1.0)
0.5	1.10	20.6	0.81	18.4(17.2±1.1)
1.0	1.10	20.3	0.80	17.9(16.3±1.3)
2.5	1.05	19.6	0.74	15.2(13.6±1.3)
5.0	1.00	18.9	0.69	13.0(11.4±1.2)

After that, Zhou's group from Hongkong fabricated a FET device based on Ag-doped $CsPbBr_3$ nanocrystals (NCs), in which the band structure and charge transport are changed by Ag doping.[51] Ag^+ ions doped into perovskite NCs are much more difficult than thin films or single crystal, which Zhou et al. adopted the hot injection method.[52] Same with Chen's results, it is proved that Ag^+ ions were doped into B-site of perovskite,

and fermi level of both materials exhibits a decreasing trend in the band structure, however, the change is from intrinsic to heavy P-type behavior in this work. After ultraviolet photoelectron spectroscopy (UPS) measurement, electrical properties are investigated as well, FET based on Ag-doped perovskite NCs semiconductor layer shows a 10^4 fold of magnitude improvement in mobility, as shown in **Figure 3(f)**. **Figure 3(b)** to **3(d)** exhibit the I-V output characteristic of the device with different doping concentrations. The current of Ag-doped devices exhibits several orders of magnitude higher than the undoped device with the same Voltage value, suggesting that the conductivity of the material is enhanced undoubtedly after doping. Furthermore, hysteresis in this FET devices could be neglected, suggesting that silver doping strategy can help to repair the trap states adequately in the $CsPbBr_3$ nanocrystals, whereas the influence of ion migration and phono scattering could be reduced as well.

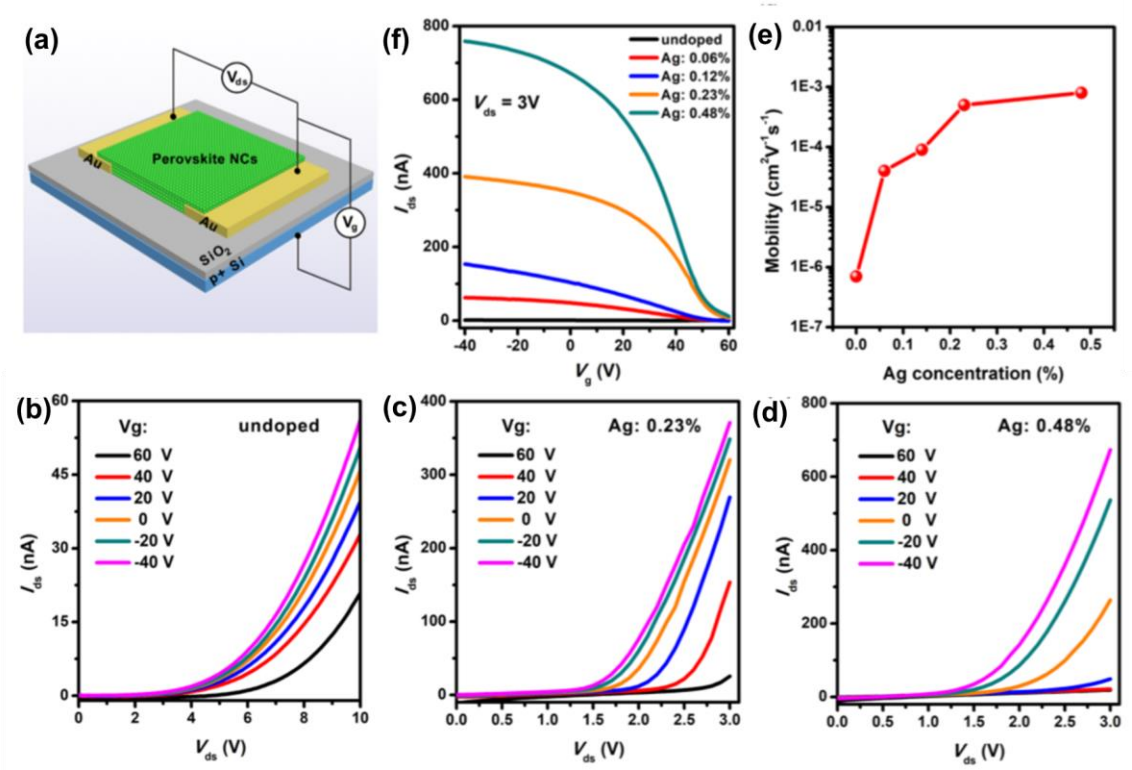

Figure 3. (a) Configuration of the FET device. Performance of field-effect transistors based on

(b) pure, (c) 0.23% (d) 0.48% silver ions doped $CsPbBr_3$ NCs. (e) Transfer characteristics of the field-effect transistors and (f) hole mobility changes with doping concentration.[51]

Two Ag-doped works were reviewed thoroughly above, which are the most relevant literature with my project. In my thesis, Ag^+ doped $MAPbBr_3$ single crystals were synthesized to investigate the different optical and electrical properties between doped and undoped one. Results and discussion will be displayed in Chapter 4.

2.2.2 B-site Divalent Ions Doped Lead Halide Perovskites

Substituting Pb^{2+} by same valence ions, called isovalent doping, in which the most potential dopant is Sn^{2+} due to its relativity with lead and non-toxic. Enormous tin-doped perovskite solar cells (PSCs) with various doping concentrations from 0 to 100% as well as lead-free are reported in the past few years.[46,53,54]

In 2014, Sn^{2+} ions were used to adjust the bandgap of $MAPbI_3$ with extending the range of absorption to the near-infrared region (NIR). However, the bandgap change with Sn concentration is not linear, as shown in **Figure 4(b)**, the narrowest bandgap is 1.17 eV when the doping concentrations are 50% or 75%. Moreover, the achievements of mixed lead and tin at B-site perovskite solar cell with organic spiro-OMeTAD/lithiumbisimide/ pyridinium additives as hole transport layer is improved as well. Although the PCE was decreased from 8.31% to 7.27% after 50% Sn doping, the absorption edge shows a near 260nm redshift to NIR, and the highest circuit photocurrent density (20.64 mA/cm^2) was collected[46]. The results were confirmed by Ogomi's work[53], in which the extension of the absorption trend was observed as well. Since the structures of PSCs in two works are different, PCE could not be compared in this situation. However, the highest J_{sc} was also

obtained by Sn-doped PSC from Ogomi's work, suggesting that Sn did help that charge transport in PSC.

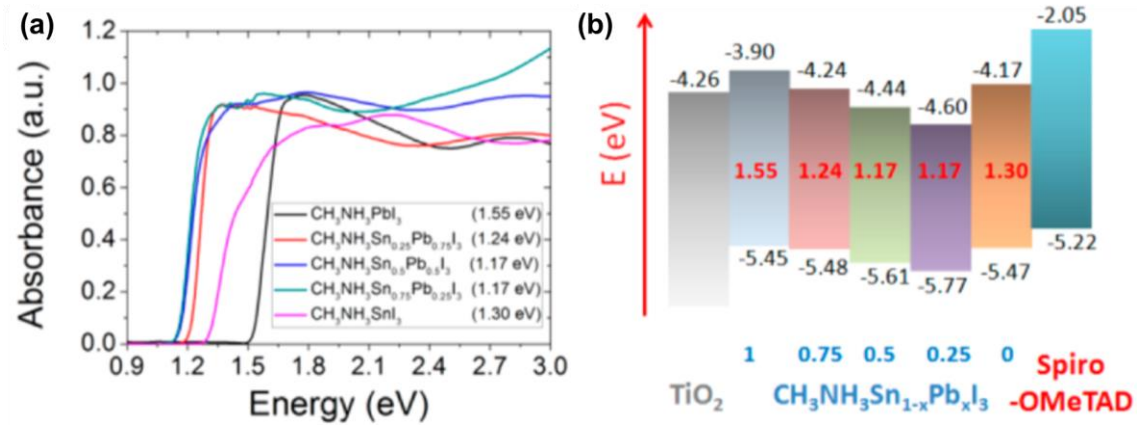

Figure 4. (a) Absorption diagram of the $CH3NH_3Sn_{1-x}Pb_xI_3$ thin films. (b) Energy level diagram of the Sn doped thin films with various doping levels measured by Ultraviolet photoelectron spectroscopy.[46]

Interestingly, the bandgap changing trend of tin doped $CsPbBr_3$ NCs is opposite with thin films. In 2016, Zhang et al. fabricated a Light emitting diode with $CsPb_{1-x}Sn_xBr_3$ NCs, with enhanced luminance and efficiency.[55] The PL peak and absorption spectra of Sn-doped perovskite NCs exhibit blueshifts, suggesting that lattice distortion due to the dopants in the NCs is different with thin films.[56] However, the luminance and current efficiency of LED devices based on undoped perovskite exhibit a 681 cd m^{-2} and 2.67 cd A^{-1} enhancement after doping with 0.3% tin ions. When the doping concentration is higher than 0.3%, the performance of the device exhibits a strikingly drop due to the large trap state density caused by the Sn impurity, indicating that optimize performance is reached by proper doping concentration. In addition to thin films and NCs, Sn doped perovskite single crystals were investigated in 2018 by Ju et al.[57] The bandgap was narrowed from 2.18 eV to 1.77 eV with 0.61% Sn doping concentration, however, the same trend

happened in single crystal, when the doping concentration excess some certain value, bandgap would exhibit an opposite changing direction, which is not linear. Moreover, As shown in **Table 2,** Sn doped perovskite single crystal shows almost 2 microsecond carrier lifetime, which is much longer c than some other perovskite single crystal.

Table 2. Carrier lifetime Sn-dope $MAPbI_3$ single crystal and other undoped perovskites single crystal

Perovskite single crystal	τ_r(ns)	τ_d (ns)	references
$MAPbI_3$		$5.7*10^5$	[58]
$MAPbI_3$	25	1100	[59]
$MAPbBr_3$	77	1000	[59]
$FA_{0.1}MA_{0.9}PbI_3$	119	1070	[60]
$MAPbI_3$	29	500	[61]
$MAPbI_3$	128	1700	[62]
$FA_{0.45}MA_{0.55}PbI_3$	119	2300	[62]
$MAPbBr_3$ powder	11	230	[57]
$MASnBr_3$ powder	320	1920	
$MAPb_{0.68}Sn_{0.32}Br_3$ powder	390	2020	
$MAPb_{0.65}Sn_{0.32}Br_3$	350	3001	

However, Sn^{2+} is easy to be oxidized to Sn^{4+} under the ambient, which impede the development of application fabricated by Sn doped perovskite. In addition to Sn, Mn as a transition metal is regarded as an alternative dopant for lead halide perovskite (LHP), two Mn^{2+} doped LHP works were published in 2016 by Liu's group and Parobek's group

synchronously.[63,64] Mn is an ideal element for adjusting the optoelectronic properties of II—VI semiconductors, which could generate sensitized Mn^{2+} luminescence. As shown in **Figure 5(a)**, $CsPbI_3$ has the most suitable bandgap for energy transfer from host exciton to Mn^{2+} d states among inorganic perovskite material system. From PL result shown in **Figure 5(b)**, Mn^{2+} doped NCs show dual-color emission, which Mn d states caused PL peak at 586 nm with yellow color (**Figure 5(c)**). Since the optical property of LHP could be altered by Mn^{2+} doping, LED based on Mn^{2+}-doped $CsPbCl_3$ was fabricated in 2017 by Liu's group.[65] Compared with undoped $CsPbCl_3$, photoluminescence quantum yields (PLQY) of Mn doped material shows an order magnitude increase from 5% to 54%. Moreover, the doped LED exhibits good stability which could work under 3.5V for 200h.

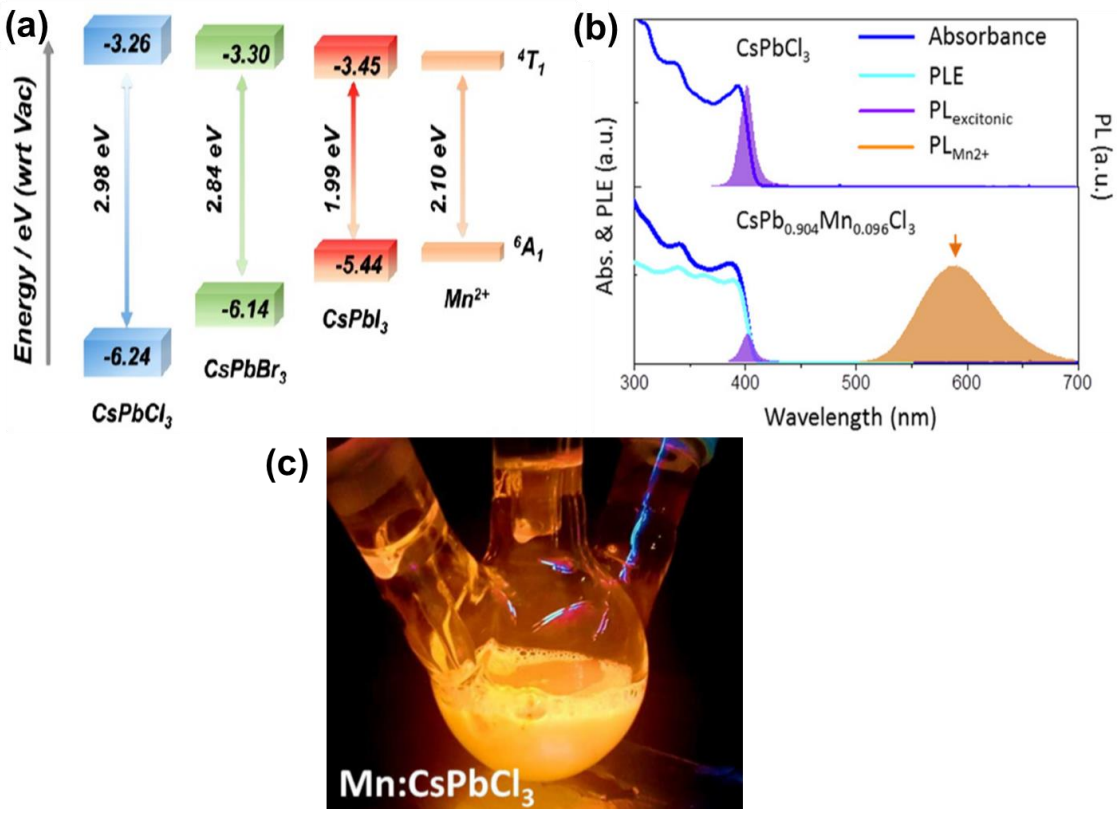

Figure 5. Energy level diagram of $CsPbX_3$ NCs and d state of manganese. (b) Absorption spectra, PL spectra and PL excitation (PLE) spectra of pure and manganese ions doped $CsPbCl_3$ NCs. (c)

Image of Mn-doped $CsPbCl_3$ quantum dots.[66]

Due to the similarity in the radius of ions, Sr^{2+} (118pm) ion is regarded as an alternative element for Pb^{2+} (119pm) replacing, which could mitigate the impact caused by lattice distortion and structure contraction. Sr^{2+}-incorporated $MAPbI_3$ thin film was synthesized in 2016[67], p-i-n planer solar cell based on this kind of thin film was fabricated as well, which the photovoltaic performance is improved. Fill factor (FF) of the Sr^{2+} doped PSC is increased from 78% to 85% after 2% Sr^{2+} doping due to the charge extraction in the solar is enhanced induced by the presence of $Sr(C_2H_3O_2)_2$. Moreover, as shown in **Figure 6**, the lifetime of charge carrier is enhanced dramatically with Sr^{2+} incorporation, which measured by time-resolved microwave conductivity (TRMC). Nearly 40 microseconds is even longer than some reported values of perovskite single crystals.[68] In addition to the lifetime of charge carriers, the recombination lifetime is increased from 11.1 ns to 17.1 ns with 2 % Sr^{2+} doping due to the passivation by the Sr-doped surface.[69] However, as we all know, after introducing with impurities, defects in the materials are formed, which could impact the lifetime of emission and trap carriers. As illustrated in **Figure 6 (c)** and **(d),** after the introduction of Sr ions, PL emission lifetime of $MAPbCl_3$ exhibits a 140 ns reduction than undoped sample.[70]

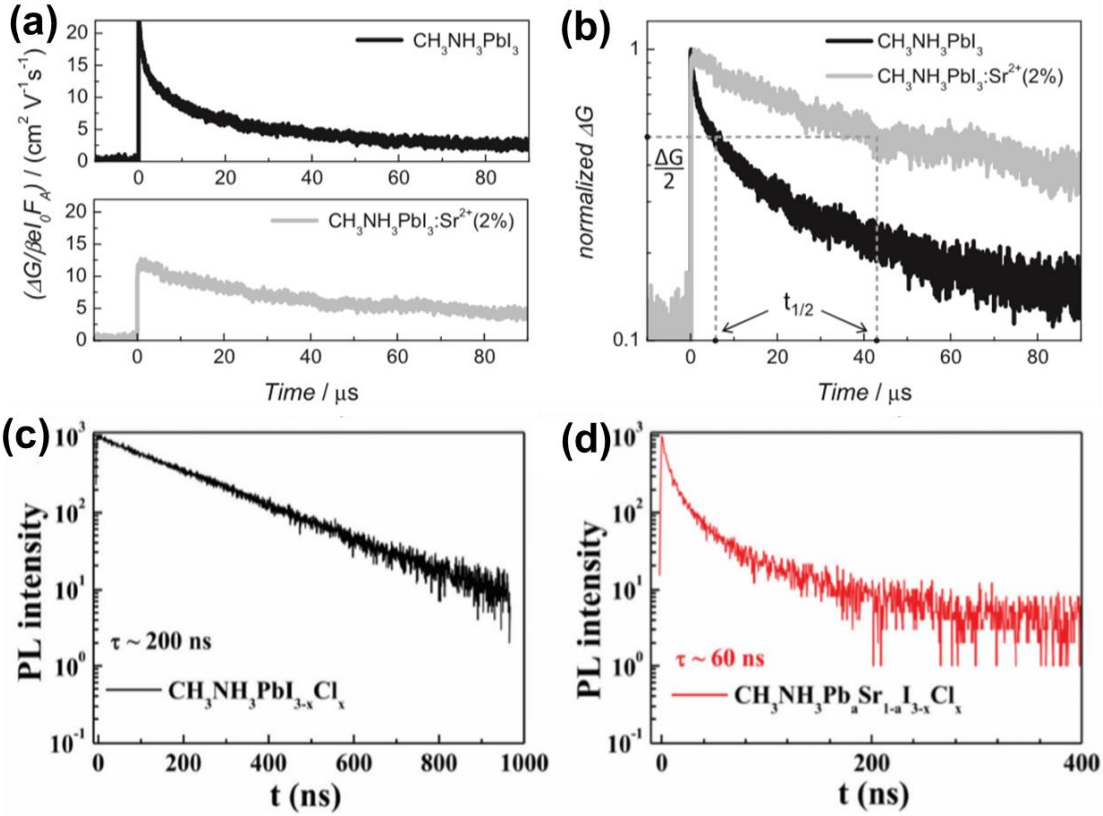

Figure 6. (a) TRMC curves for the pure and strontium doped $MAPbI_3$ thin films (b) Normalized TRMC curves of the pure and strontium doped samples.[67] Time-resolved PL decay spectra of pristine(c) and Sr-doped $MAPbCl_3$(d) sample.

Another alkaline metal ion, Ba^{2+} is also regarded as a potential substitute for the lead base in LHP, in which the optoelectronic properties could be altered. The facts that morphology and quality of $CH_3NH_3PbI_3$ thin films are enhanced with Ba^{2+} introduction is proved by Chan et al. in 2017.[71] Since the crystallinity of Ba-doped thin film is increased, thus, charge carrier transport ability of the thin films is enhanced as well, which affect the photovoltaic performance of PSCs based on this kind of material. Moreover, with the smaller electronegativity compared with Pb^{2+}, Ba-I bonds are stronger than Pb-I bonds, leading to better stability than undoped PSC. First-principles calculations were applied to explore the change in the bandgap of Ba-doped material[72]. As shown in **Figure 7**, the

bandgap is ranging from 1.56 eV(undoped) to 4.08 eV (100% Ba^{2+}-doped), which is consistent with experimental results, suggesting that optical properties could be adjusted by Ba-doping. Consequently, Ba^{2+}-doped $MAPbI_3$ thin film was used as the capping layer in PSC, an outstanding PCE (18.9%) is reached with over 30 days of long-term stability. In this part, LHP family B-site doping works with divalent ions like Sn^{2+}, Mn^{2+}, Sr^{2+}, Ba^{2+} are briefly introduced with basic achievements after doping. There are some other elements like Ca[73], Cd[56], Zn[56], Mg were used as dopants for LHP as well, because the results are not that promising, these works are not mentioned in this part.

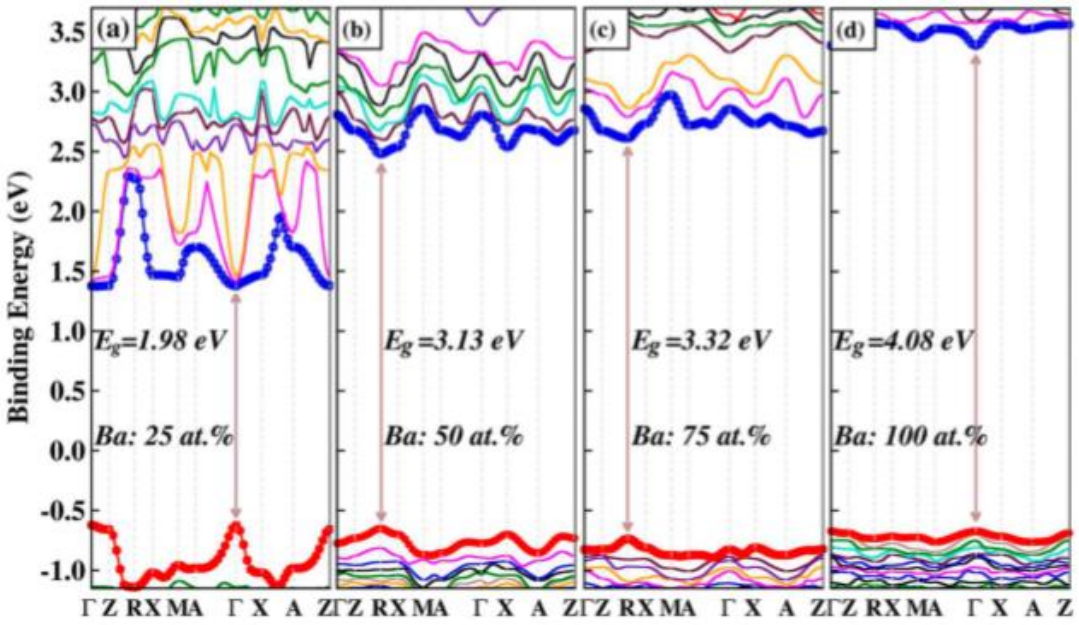

Figure 7. Calculated band structures of the Ba-doped $MAPbI_3$ with different doping concentration (a) 25%, (b) 50%, (c) 75%, (d) 100%.[72]

2.2.3 B-site Heterovalent Ions Doped Lead Halide Perovskites

The most intensively studied heterovalent ion for doping work into LHP is Bi^{3+}, numerous articles of Bi^{3+} doping lead halide perovskites family have been reported over the last few years. Among these publications, investigation of Bi^{3+} doped $MAPbBr_3$ single crystal

from Abdelhady et al. is the first choice for reviewing.[74] Bi^{3+} doped single crystals were synthesized from precursor with $BiBr_3$, and the color of Bi-doped single crystal becoming dark with doping concentration increase, as shown in **Figure 8(a)**. Bandgap narrowing (BNG) has also happened on Bi^{3+} doped single crystal, which the bandgap declines from 2.08 eV to 1.89 eV after doping 10% Bi^{3+}. (**Figure 8 (b)**) More interestingly, as an intrinsic p-type semiconductor, the introduction of Bi^{3+} ions enables the majority carriers of undoped single crystal switch to positive carriers. As shown in **Figure 8 (c)**, enhancement of electric properties after doping with bismuth is exhibited on carrier concentration and conductivity, which are increased three and four orders of magnitude, respectively.

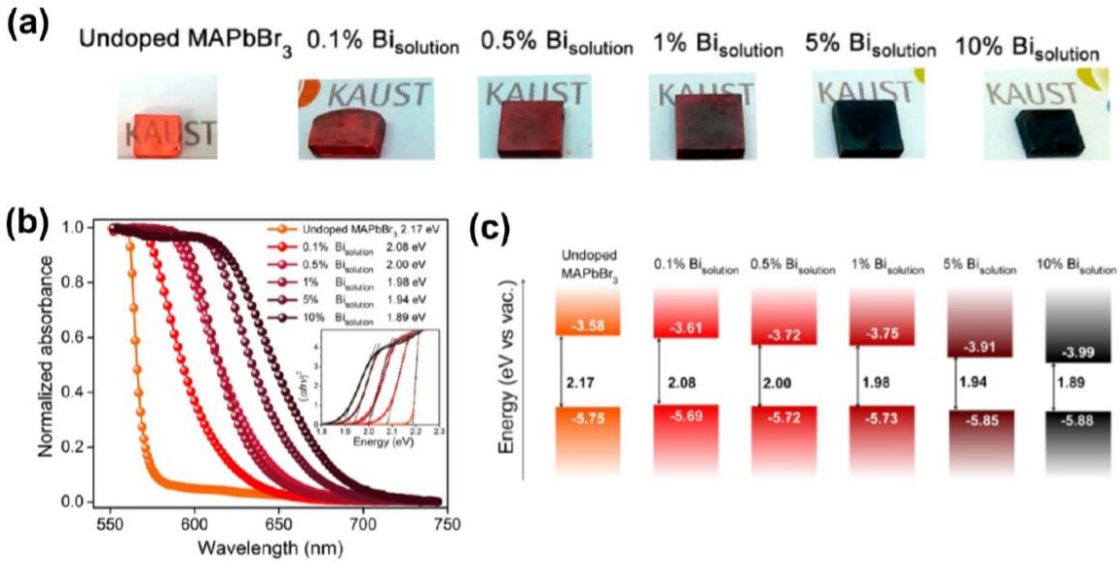

Figure 8. (a) Digital images of Bi-doped single crystals with ordered Bi doping concentration from 0% to 10%. (b) Absorption spectra of the same samples in (a). Inset: Binding energy of each sample (c) Conductivity and charge carrier concentration of the samples against with composition of Bi in the B-site.[74]

Since the ion radius of bismuth ion is 16 pm different from that of lead ion, the

introduction of Bi^{3+} may cause lattice distortion in the host and the defects are increased as well, leading ultrabroad emission induced by coupling effect of excitons and crystal lattices. After doping with Bi^{3+}, defects in the surface of $MAPbI_3$ thin film increased, thus, PL intensity exhibits quenching effects. As displayed in **Figure 9(a)** and **(b)**, PL peak in 780 nm decrease constantly with Bi^{3+} doping concentration increase, emission band was broadened to NIR region at around 1140 nm, which originated from Bi-doping luminescent center induced by the coupling effect between PbI_6 octahedral and spatially localized bipolarons.[75]

In addition to LHPs thin films and single crystals, Bi doping in LHPs NCs is also investigated and exhibits different band alignment with single crystals.[76] As displayed in **Figure 9 (c)** and **(d)**, the first excitonic absorption peak doesn't exhibits monotonously shift, which it shifts to lower energy at 0.25% Bi-doping and shifts to higher energy at higher doping concentration, suggesting that successful incorporation of bismuth ions into the $CsPbBr_3$ NCs. Moreover, Fermi level of $CsPbBr_3$ NCs has confirmed the location where near the Valence Band (VB) but it is shifted up to Conduction Band (CB) after the introduction of Bi^{3+}, indicating the existence of Bi doping in crystal lattice. To explain the abnormal shifts in PL spectra, band alignment of Bi-doped $CsPbBr_3$ NCs is depicted in **Figure 9 (e)**. After a large number of dopants are introduced, Conduction Band receives excess electrons from dopants resulting a wider bandgap attributed to the higher CB, which also known as Burtein-Moss effect.[77] Furthermore, due to the variation of band structure, carrier recombination is delayed by it, causing increment on the recovery time of Bi-doped $CsPbBr_3$ NCs.

Among all the highlights of Bi-doped publication, bandgap narrowing is mentioned most, however, a recent study claimed that BGN doesn't occur on Bi-doped $CsPbBr_3$ single crystals.[78] Peaks of excitonic luminescence various doping level samples exhibit a stable position without shift. UPS measurement indicates the Fermi level and VB of samples remain unchanged with different doping concentrations. This debate about if BGN occurred on Bi-doped LHPs is continuing, and more data are needed to support this conclusion.

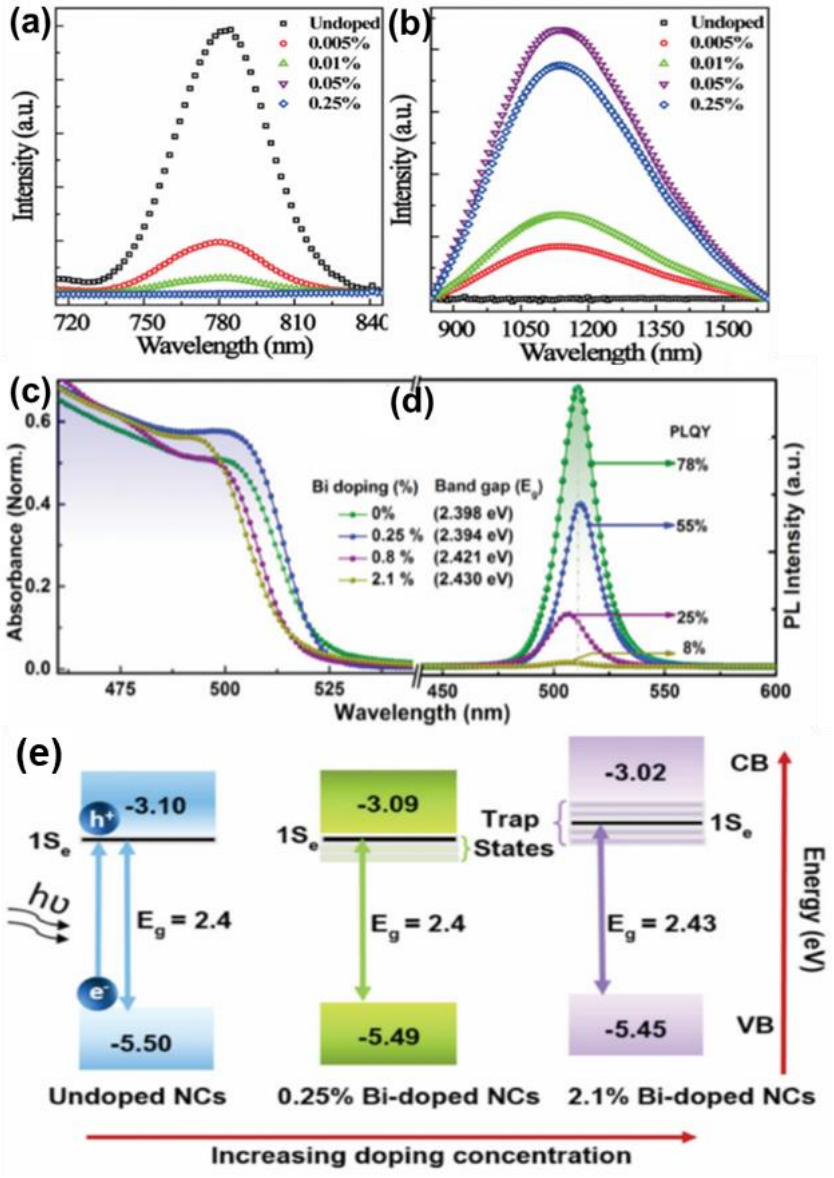

Figure 9. PL spectra of pure and Bi^{3+}-doped perovskites with various doping levels (a) (b). (c) Absorption spectra an (d) PL spectra of pure and Bi^{3+}-doped $CsPbBr_3$ NCs.[75](e) Band alignment of $CsPbBr_3$ NCs after doping with different Bi^{3+} concentration.[79]

In addition to Bismuth, heterovalent ions like Al^{3+}, Fe^{3+}, $Sb^{3+,}$ and In^{3+} are also investigated as dopants for LHPs.[80-83] $CsPbBr_3$ NCs has been used as host for several elements doping work as we mentioned above, its optical properties are easy to be adjusted upon doping. As an earth-abundant element, Aluminum is also in the list, stable blue photoluminescence is achieved by Al-doped $CsPbBr_3$ NCs reported from Lie et al. in 2017.[80] As shown in **Figure 10(a) (b)**, because the quantum confinement is enhanced upon doping, both the absorption peak and PL exhibits a 75nm blue shift, along with the reduction on the PLQYs of Al-doped nanoparticles (NPs). Moreover, according to the Time-resolved photoluminescence (TRPL) measurement, PL lifetime of Al^{3+} incorporated NCs is shorter than the undoped attributes to the energy transfer between Al^{3+} and perovskites. In terms of device performance, white-light-emitting diodes (WLED) based on Al-doped $CsPbBr_3$ NCs show over 100% efficiency on National Television System Committee (NTSC), which is higher than the previous report.

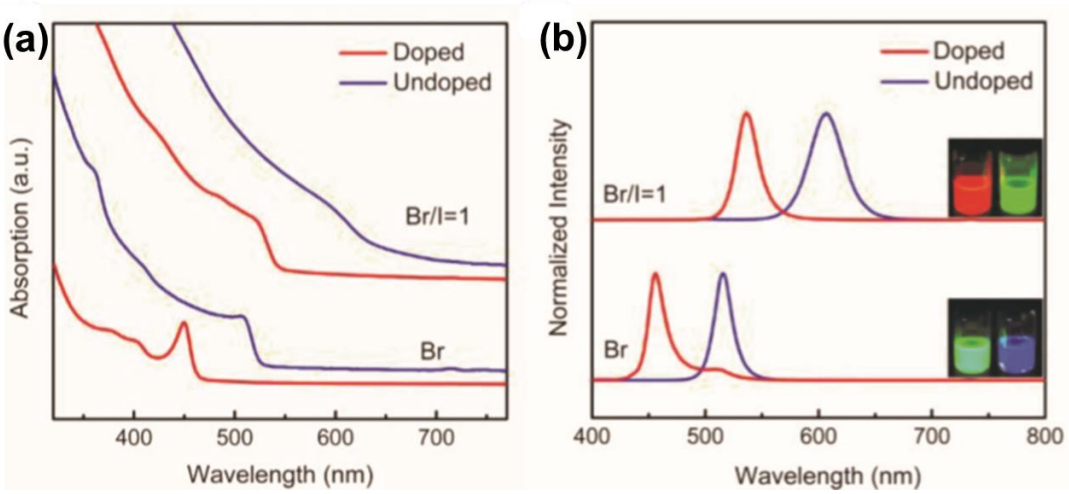

Figure 10. (a) Absorption spectra and (b) PL spectra of pure and aluminum incorporated $CsPbBr_3$, $CsPbBr_xI_{3-x}$ samples. Insets are digital images of the pure and aluminum incorporated NCs under WLED.[80]

As an inevitable impurity in ambient, Iron ions with various valance are introduced into LHPs to explore the photoelectric properties. Recently, photodetector based on Fe^{2+}/Fe^{3+} doped $MAPbCl_3$ single crystals was fabricated[81], however, the performance of the device is not enhanced as expected. Fe^{2+} replaced Pb^{2+} in the LHPs, optoelectronic properties are degraded upon doping, causing lower photocurrents and on/off ratio of the photodetector. Moreover, dark current of Fe^{3+} doped device exhibits ten times higher than the undoped sample, implying plenty of MA^+ vacancies are created upon Fe^{3+} A-site doping. Therefore, both Fe^{2+}/Fe^{3+} are not appropriate dopants for LHPs applications.

Indium and antimony as two post-transition metallic elements which locates diagonally adjacent to Pb are used as dopants for hybrid halide perovskites solar cell.[82,83] $MAPbX_3$ thin films with hybrid halogen Cl and I are used as hosts for In and Sb doping works. With the assisted by Sb^{3+}, short-circuit current density (J_{sc}) of PSC rises from 16.8 mA cm^{-2} to 20.9 mA cm^{-2} and good stability is showed within 28 days. Moreover, FF and photocurrent conversion efficiency are enhanced induced by the creation of a homogeneous microstructure of SbI_3 assistted with NH_4Cl. Similar results are also collected from In^{3+} doping PSC, after incorporating 0.15% In in the B-site, forming a Pb-In binary system, the highest J_{sc}, FF and PCE of In-doped PSC are reached, which are 21.90 mA cm^{-2}, 0.78 and 17.55%, correspondingly. The improvement of application performance could be explained by the morphology and crystallinity of In-doped

perovskites thin films is improved, resulting in a higher charge transport efficiency, which is beneficial for the electrical performance of the solar cell.

Several heterovalent doping works are reviewed in this part, indicating it is a feasible path to adjusting the electrical and optoelectronic properties of LHPs as well, performance of doped LHPs applications could be improved as expected.

2.3 Review Summary and Project Scopes

In this chapter, plenty of B-site doping with various valence metal or post-transition metallic ions investigations in recent years are reviewed. Whether the host is single crystals, polycrystalline thin films, or NCs, the introduction of dopants can bring the variation on crystallinity, morphology, crystal structure, optical and electronic properties of LHPs, resulting in improvement or decrement of the performance of doped LHPs applications. There is no doubt that dopant engineering has become an effective strategy for adjusting the properties of halide perovskites, attracting more attention to this outstanding material.

Although B-site doping has achieved gratifying achievements so far, there is still a series of questions waiting to be explained, such as the relationship between distorted crystal structure and properties of the doped perovskites, the interaction between host and dopants, mechanisms for bandgap adjustment after doping, etc. Therefore, it is necessary to accurately analyze the basic characterization results of doped samples, and even some small changes should be given proper attention. Bandgap tailoring is the most alluring target for doping engineering, interactions between dopants and host should be investigated particularly to obtain optimal optical properties. However, the stability of

doped LHP is still a huge stumbling block on pursing desired doped-induced optoelectronic properties, improvement on stability should be a major target of the development of doping engineering in the future.

After reviewing plenty of publications above, basic understandings on B-site doping works are known. Herein, the scope of this project will be briefly introduced. In this work, Ag-doped $MAPbBr_3$ single crystals were synthesized by a modified growth method and its optical properties and electrical properties were investigated. As we all know, single crystal is an optimal platform to investigate basic physical properties of LHPs, with no grain boundaries and morphological issues. Moreover, compared with polycrystalline thin films, single crystals exhibit better electrical properties as well, which are longer diffusion length, lower trap-state density and higher charge-carrier (hole/electron) mobility.[59,84] Therefore, $MAPbBr_3$ single crystal is used as host to investigate the effects of Ag-doping in terms of optical and electrical. The experimental procedure and results will be discussed in Chapter 3 and Chapter 4.

Chapter 3 – Experimental Procedure and Methods

3.1 Preparation of Samples

In this work, Ag-doped $MAPbBr_3$ single crystal is the core object which has been investigated thoroughly. To better investigate the single crystal, high quality samples are needed, in which could be synthesized in several ways. Herein, diverse single crystal growth methods will be reviewed below, the modified method employed in this work will be described after the review.

3.1.1 Reviews of Lead Halide Perovskite Single Crystal Synthesis Methods

Nowadays, due to its simplicity, low cost and adaptability, solution process growth methods attract more attention than Bridgemen method, which is used for growing inorganic perovskite single crystal such as $CsPbBr_3$.[85] Since $MAPbBr_3$ single crystals used in this project is categorized as hybrid organic-inorganic perovskites, only several solution-processed growth methods will be focused in this part.

Solution temperature lowering (STL) is one of the traditional methods of synthesizing HOIP single crystals. MA-based perovskite single crystal was growtn by Poglitsch in 1987.[86] In this way, saturated precursor is prepared at high temperature, and will be placed into fume hood until small crystal seed appears. Since the temperature distribution in the precursor is not uniform, thus, bottom and top-seeded solution growth (BSSG, TSSG) are invented based on the traditional STL method. As shown in **Figure. 11(a)(b)**, a large $MAPbI_3$ single crystal with 10 mm * 10 mm * 8mm size grew from small $MAPbI_3$ single crystal seed with high quality by using the BSSG method.[87] After put the small seed into the new saturated precursor, temperature around the flask is turned down from 65℃ to 40℃, resulting in the precipitation of large single crystal which the process could last for a month. Compared with BSSG, the TSSG method requires more specific temperature control and more complicated equipment. In this method, several small single crystals will be settled on the silicon substrate at the bottom of the bottle with around 75 ℃. Since the hot plate is assembled under the bottle, temperature of the top area of the bottle is lower than the bottom, resulting in minor temperature discrepancy in the bottle. Thus, small single crystals in the bottom could supply the ions for the saturation precursor

located in the bottom which makes the precursor in the top area could be supersaturated, providing enough ions for large crystal growth. Consequently, the largest $MAPbI_3$ single crystal grew from TSSG is around 10mm* 3mm with relatively high quality. The digital image of $MAPbI_3$ single crystal is shown in **Figure 11(c)**, and the configuration of TSSG is illustrated in **Figure 11(d)**. Despite high quality HOIP single crystals were synthesized by STL, it could not be used as an effective way due to its time-consuming problem, which could spend couple of weeks to grow one satisfactory crystal.

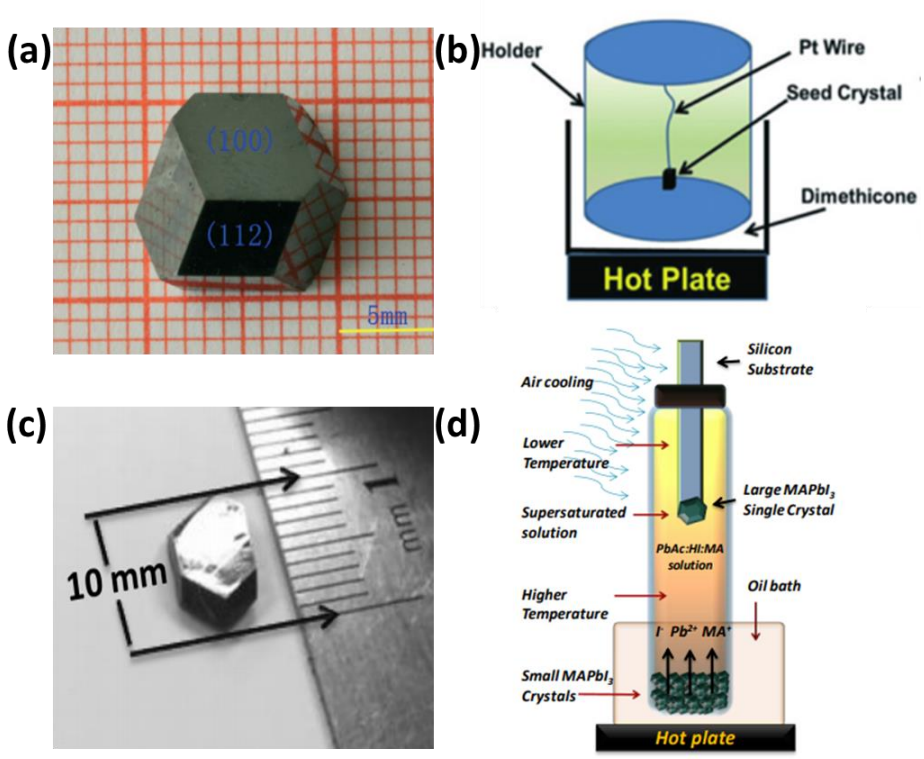

Figure 11. (a) Digital image of $MAPbI_3$ single crystal with (100) and (112) facets. (b) Schematic illustration of BSSG method. (c) Digital image of $MAPbI_3$ single crystal synthesized by TSSG method. (d) The set-up of TSSG method.

To overcome the time-consuming problem, the rapid crystal growth method is reported by Bakr et al. in 2015[88], which named inverse temperature crystallization (ITC). Some HOIP exhibits retrograde solubility in particular solvent like γ-butyrolactone (GBL) for

$MAPbI_3$, N, N-dimethylformamide (DMF) for $MAPbBr_3$ and dimethylsulphoxide (DMSO) for $CsPbBr_3$, which temperature increment could result in the decrement on solubility. Centimeter-sized $MAPbX_3$ single crystals will be synthesized by ITC methods within hours, in which the fastest growth rate of $MAPbBr_3$ single crystal could be 38 mm^3 h^{-1}. GBL and DMF are used as solvent to dissolve $MAPbBr_3$ and $MAPbI_3$ precursors with 1 mol L^{-1}, respectively. Oil bath is recommended to be used during temperature rise-up, which could realize uniform heating process. **Figure 12 (a)(b)(c)** illustrate the process by design sketch and real images. Despite the rapid growth speed, drawbacks of ITC methods still exist, which the size of single crystal is relatively small. Thus, a modified ITC method which can obtain high quality and large size single crystal namely low-temperature-gradient crystallization (LTGC) is reported by Liu et al. in 2019.[89] According to the solubility measurement of $MAPbBr_3$ in DMF, authors discovered that temperature range where the solubility changes the most is from 25℃ to 60℃, which the temperature against concentration curve is shown in **Figure 12.(d)**. It has been demonstrated that temperature act a crucial character in crystal synthesizing, in which the crystallization yield and crystal quality are determined by it. Therefore, selected crystal seed is put into fresh precursor above the hot plate with 25℃. Temperature of hot plate increase with an increased rate of 2℃ per 24 hours, precursor will be filtered every 24 hours. Consequently, a high quality $MAPbBr_3$ single crystal with 47mm * 41mm *14mm size was synthesized, the digital image is shown in **Figure 12(e)**. However, spending almost 20 days for growing one large single crystal is not smart, thus, ramp rate could be accelerated to 3℃ /day, which adopted by Cheng et al.[90] As shown in **Figure 12(f)**, high quality $MAPbCl_3$

single crystal is obtained by modified LTGC method, exhibiting better optoelectronic properties than other reports. In summary, ITC method could be modified into various versions to meet the requirements of various applications. Theoretically, infinite size single crystal could be synthesized if the precursor could be updated periodically.

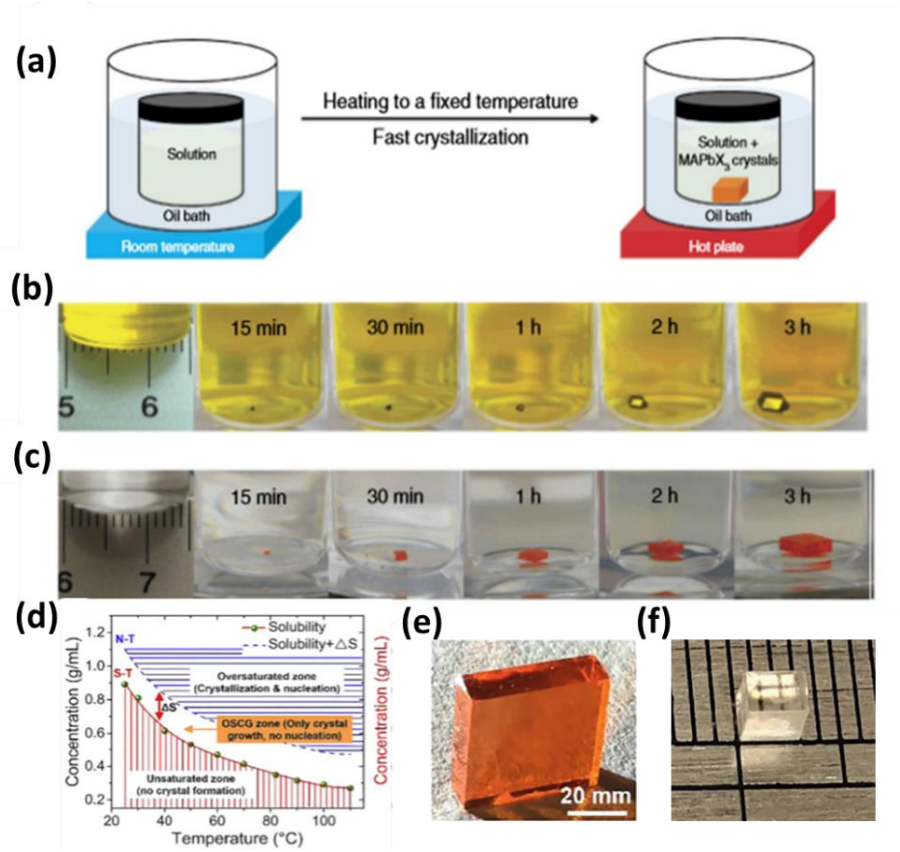

Figure 12. (a) Schematics depict the procedure of ITC method. (b)(c) The gradual growth of $MAPbBr_3$ and $MAPbI_3$ single crystal at different time intervals, respectively. (d) Solubility traces and concentration against temperature in various districts. (e)(f) Photo of $MAPbBr_3$ and $MAPbCl_3$ single crystal obtain by LGTC method, respectively.

However, temperature is a tricky variable to be controlled specifically even with oil bath. Temperature-independent method known as antisolvent vapor-assisted crystallization (AVC) method was established. Since HOIPs exhibit different solubility in various solvents, solvent with low or non-solubility of HOIPs could help the synthesizing of

single crystal from precursor, which the solvent called antisolvent. As shown in **Figure 13(a)**, the vessel contained precursor is surrounded by antisolvent, which placed in a sealed flask. Crystallization is started when antisolvent flow to the vessel slowly and it will cost several days until millimeter-sized single crystals are collected. Dichloromethane (DCM) is the most common antisolvent for HOIP single crystal synthesis, especially for $MAPbX_3$ single crystals.[59] $MAPbX_3$ single crystals with low trap density and long diffusion length are obtained, indicating AVC is a feasible way to synthesize high-quality single crystals. Until now, various HOIP single crystals were synthesized through AVC method, selected pictures of single crystals are displayed in **Figure 13(b)(c)(d)**. In general, since AVC is a temperature-independent method, allowing the neglect of phase transition of single crystal induced by temperature and thermal convection on neatly single crystals. Same with STL method, time-consuming could impede the development of AVC method as well.

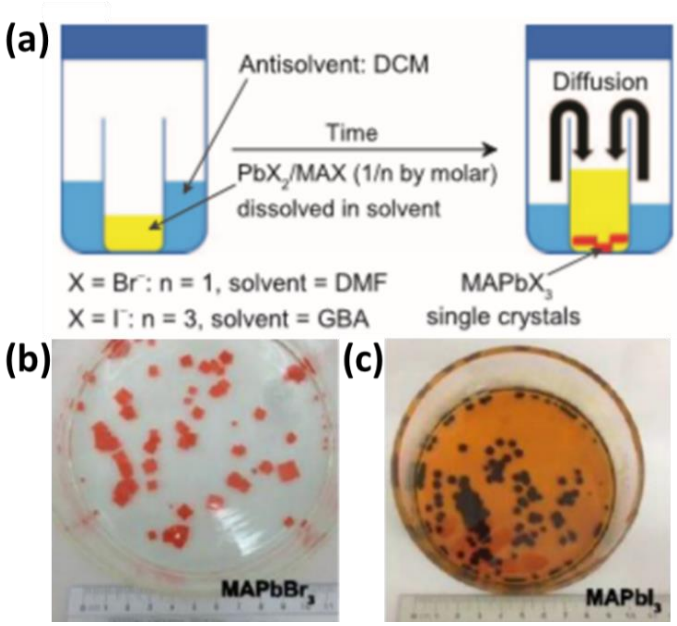

Figure 13. (a) Schematic diagram of AVC method process (b) (c) Photo of $MAPbBr_3$ and $MAPbI_3$ single crystals *via* AVC method.

Single crystal synthesis methods are reviewed above, solution-processed low-cost methods have replaced traditional methods, becoming the mainstream methods adopted by researchers progressively. After reviewing methods, some parameters of HOIP single crystals are summarized in **Table 3.** In this project, the modified ITC method was employed to synthesize pure and Ag-doped $MAPbBr_3$ single crystals. More details will be introduced in the next part.

Table 3. Summary of HOIP single crystals parameters

Single crystal	Crystal size /(mm*mm*mm)	Trap density/ ($10^{10}cm^{-3}$)	Mobility/ ($cm^2V^{-1}s^{-1}$) holes	Lifetime/ns		Diffusion Length/μm		Ref.
				Fast	slow	shorter	longer	
$MAPbCl_3$	2*4*4	3.1	42	83	662	3.0	8.5	15
$MAPbBr_3$	47*41*14	0.67	83.9	132	897	5.3	13.8	89
$MAPbBr_3$	44*49*17	0.62	81	139	899	5.4	14.2	91
$MAPbI_3$	~ 10	4.5	164	95	82	-	175	84
$MAPbI_3$	71*54*39	2.6	34	-	-	-	-	92
$MAPbI_3$	9	0.31	162	-	-	-	-	93
$MAPbI_3$(Cl)	20*18*6	0.076	167		449000	-	-	58
$FAPbBr_3$	4 - 5	0.96	62	687	2272	10.5	19.0	94
$FAPbI_3$	4 - 5	1.1	35	32	484	1.7	6.6	94
$CsPbBr_3$	3*2*1	4.2	11	23	233	5.5	2.5	18

3.1.2 Modified Version of Synthesis Method

As we discussed above, ITC can be modified as a core to achieve the desired purpose. Compared with ITC method, less time-consuming and chemical-consuming synthesis method is preferred in this project to obtain high-quality $MAPbBr_3$ single crystals to used as host for Ag-doping. Thus, low-temperature with high-molarity crystallization method (LTHMC) is employed in this work. Two steps are parted in the process.

Same with LTGC method, small and neat $MAPbBr_3$ single crystal seeds are needed to synthesize high-quality single crystals with adequate size. 10 ml 1.0 M $MAPbBr_3$ precursor is prepared by MABr (98% Sigma) and $PbBr_2$ (99% Sigma) in 1:1 ratio, specific weight for two components are 1.12g and 3.67g. Powders of two components are added into DMF (99.8% Sigma) and the solution will be dissolved after 3h magnetic stirring. PTFE filters with 0.45 micrometer pore size are used for excluding the impurities surrounded by solution to obtain transparent precursor, which is transferred to a clean beaker. Temperature of the hot plate is set as 60℃ at the beginning and will increase to 80℃ within three hours. Small and neat $MAPbBr_3$ single crystal seeds are appeared at the bottom of the beaker with almost same size. Before picking up adequate seeds, a syringe with a needle is used for drawing residual precursors out of the beaker, avoiding the damages on the seeds caused by unsaturated precursors. Moreover, filter papers are needed to wipe up the surfaces of seeds as well. As shown in **Figure 14(a)**, Selected seeds will be placed in the fume hood, waiting for the further growth process.

According to the solubility diagram, 1.85 M is the maximum molarity of $MAPbBr_3$ precursor at room temperature, which means small seeds will not dissolve in the precursor

with that high-molarity, resulting in further crystal growth of seeds. To prepare 2 ml 1.85 M $MAPbBr_3$ precursor, 0.4144 g MABr and 1.358 g $PbBr_2$ are dissolved in 2 ml DMF, with 24 hours stirring by magnetic bars. Stirring precursor by magnetic bars is beneficial for dissolving precursor completely. When the precursor dissolved completely, the PTFE filter with 0.45 μm pore size is used again for filtering impurities. As shown in **Figure 14(b)**, 2 ml high molarity precursors are poured to a clean beaker containing a selected single crystal seed with the best condition of all. The beaker is placed on the hot plate with 25℃ in the first 24 hours, following with a slow ramp rate of 2.5℃ per day. Moreover, the former precursor will be updated by fresh precursor when the temperature is turned up every 24 hours. (**Figure 14 (c)**) Consequently, $MAPbBr_3$ single crystal with perfect cubic shape and centimeter size is synthesized in the beaker within three days.(**Figure 14 (d)**) During the further growth step, the highest temperature used is around 30℃ which could be considered as low temperature, and precursor with 1.85 M is regarded as high molarity solution, thus, this modified method could be called as low-temperature high molarity crystallization method. Ag-doped $MAPbBr_3$ single crystals are synthesized *via* LTHMC with less time-consuming. More details will be introduced below.

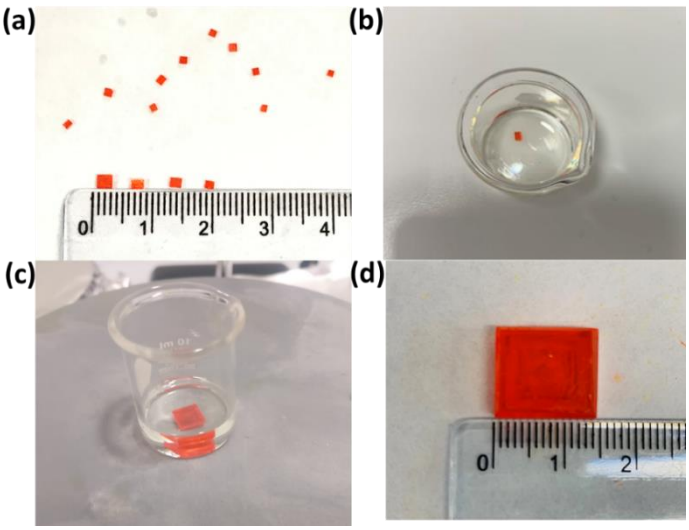

Figure 14. (a) $MAPbBr_3$ single crystal seeds obtained in the first step of LTHMC. (b) High molarity precursor containing small $MAPbBr_3$ single crystal seed. (c) Grown single crystal after the first 24h with fresh precursor. (d) Large $MAPbBr_3$ single crystal obtained by LTHMC method with 14mm * 13mm * 5mm size.

3.1.3 Synthesis of Ag-doped Perovskite Single Crystal

Since two publications of Ag-doping perovskite work have already proved that Ag will substitute B-site of perovskite which is lead instead of A-site cation. More evidence will be displayed in the next chapter. Therefore, we assume that the chemical formula of Ag-doped $MAPbBr_3$ is $MAPb_{1-x}Ag_xBr_3$, which is adopted to calculate the weight of each chemical will be used. In this project, 0%, 1%, 3%, 5%, and 10% Ag-doped $MAPbBr_3$ single crystals are needed, hence, beakers contained $MAPb_xAg_{1-x}Br_3$ precursor with different doping level as well as X value are needed to prepare. When the X values are 1, 3, 5, 10, AgBr powders needed are 0.0070g, 0.021g, 0.035g, 0.07g, respectively. After adding of AgBr, transparent precursor exhibits slight yellow color gradually with Ag doping levels increasing, change in precursor color are shown in **Figure 15(a)**. To investigate physical properties of Ag-doped single crystal, appropriate size is needed which could be suitable for characterizations and measurements. Thus, five single crystals with various doping levels are controlled in the size of 5mm *5mm. **Figure 15(b)** displayed these single crystals orderly from left to right with doping level increases, in which the size of five single crystals is basically same. Herein, to synthesize Ag-doped single crystals with same size which is around 5mm * 5mm, time spent on step 2 of LTHMC method will be shortened to 24h. It is worth noting that the surfaces of 10% Ag-

doped single crystal is not as smooth as other samples and worse stability, signifying the doping limitation of Ag ions in perovskites. More evidence will be displayed in Chapter 4.

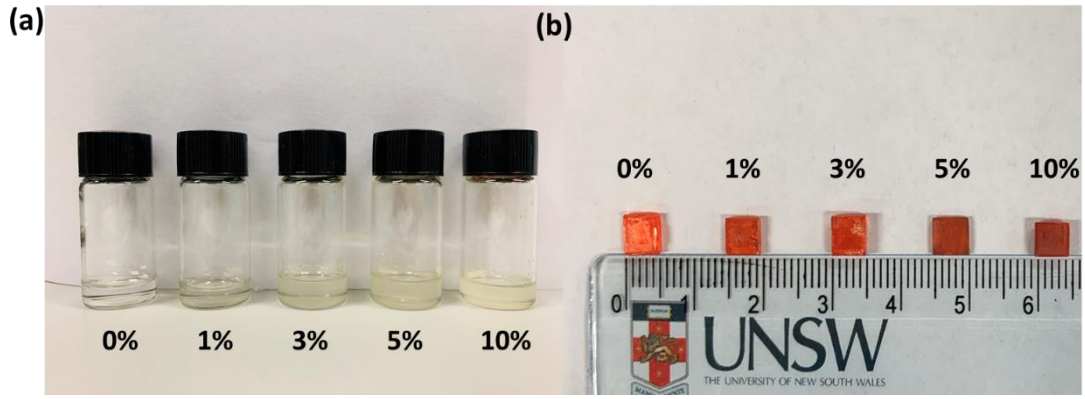

Figure 15. (a) Ag-doped $MAPbBr_3$ precursor with different Ag doping level. (b) Photos of $MAPbBr_3$ single crystals with various Ag^+ doping levels (0, 1%, 3%, 5%, 10%).

3.2 Single Crystal Characterizations

3.2.1 X-ray Diffraction (XRD)

XRD is a research method that obtains information like the components of the material, the structure, or morphology of atoms or molecules inside the material by analyzing its diffraction pattern. When a monochromatic X-ray is irradiated on the crystal, the electrons around the atoms in the crystal are vibrated by the periodically changing electric field of the X-ray, so that each electron becomes a secondary wave source that emits spherical electromagnetic waves. The frequency of the emitted spherical wave is consistent with the incident X-ray. Due to the periodicity of the crystal structure, the scattered waves of each atom (electrons on the atoms) in the crystal can interfere with each other and be superimposed, which is called coherent scattering or diffraction. Since the permutation of atoms inside the crystal is exclusive, the corresponding diffraction pattern is fixed. By

analyzing its diffraction pattern, the corresponding crystal structure can be known. Different unit cell parameters can show different diffraction peak distributions, and the type and position of atoms could affect the intensity of the diffraction peaks. To satisfy the basic conditions of diffraction, Bragg's law is proposed, which reflects the relationship between the direction of the diffraction line and the crystal structure. The equation of Bragg's Law is:

$$2d \cdot sin\theta = n\lambda (2)$$

where θ is the angle of incidence, d is the distance between crystal planes, n is the order of diffraction, λ is the incident wavelength, and 2θ is the angle of diffraction. **Figure 16(a)** shows the illustration of Bragg's law.

Since the samples used in this project are bulk, which is not compatible with thin film XRD instrument. Thus, powder XRD instrument is adopted in this project, in which the single crystals have to be ground to powders first (**Figure16(b)**). Among instruments in XRD lab, MPD (PANalytical) Xpert Multipurpose X-ray Diffraction System (**Figure 16(c)**) is the most appropriate one for powders measurement, which Cu K-α is used as X-ray energy.

Furthermore, without completely crushing the single crystal, a tiny piece of a single crystal can be measured directly through Bruker D8 Venture X-ray diffractometer (**Figure 16 (d)**), which is used for detecting crystal structure and lattice parameter of crystal.

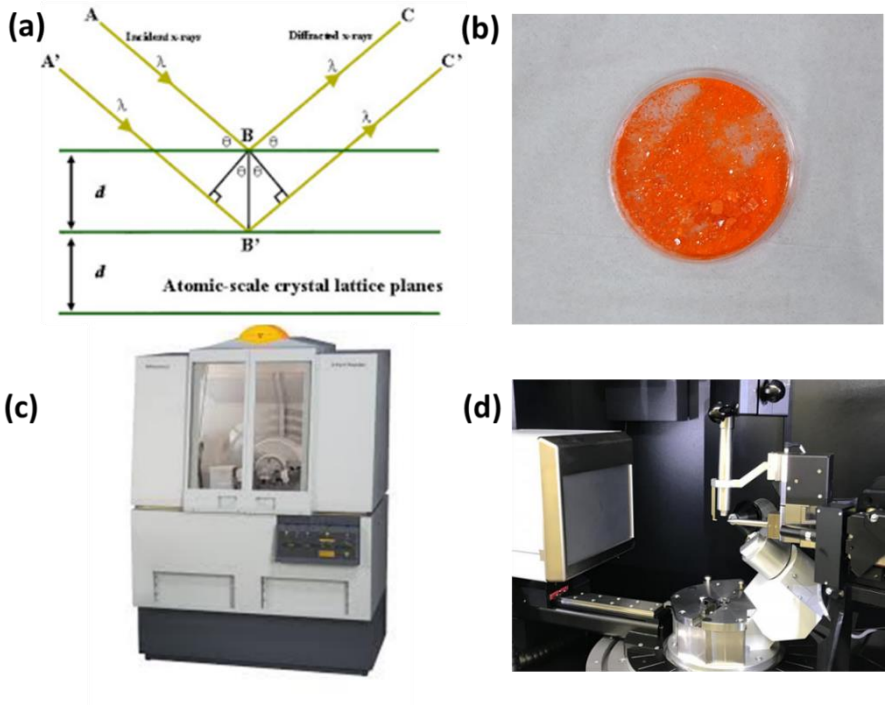

Figure 16. (a) Schematic illustration of Bragg's law in terms of atomic-scale single crystal layer plane. (b) Powder sample for MPD XRD system. (c) Photo of MPD (PANalytical) Xpert Multipurpose X-ray Diffraction System. (d) Photo of Bruker D8 Venture X-ray diffractometer used in the XRD laboratory.

3.2.2 Ultraviolet–visible (UV-Vis) Absorption spectroscopy

The absorption spectra are essential that the molecules and atoms in the material absorb the light energy of certain specific wavelengths in the incident light, and the molecular vibrational energy level transition and the electronic energy level transition occur accordingly. Since various substances have their different molecules, atoms and different molecular space structures, their absorption of light energy will not be the same, especially in the semiconductor materials. Bandgap of semiconductor could be calculated from absorption spectra, which could be the main function of absorption spectra. According to Tauc's theory,[95] bandgap of materials could be calculated:

$$(\alpha h\nu)^{\frac{1}{n}} = A(h\nu - E_g) \quad (3)$$

where α is absorption coefficient, h is Planck constant, ν is the frequency, and A is the constant. N is determined by the type of semiconductor, which is 0.5 and 2 for direct bandgap and indirect bandgap materials.

In this project, Lambda 1050 | UV/Vis/NIR Spectrophotometer (**Figure 17**) is used for testing absorption spectra of Ag-doped single crystals with measures range from 175 nm to 3300 nm.

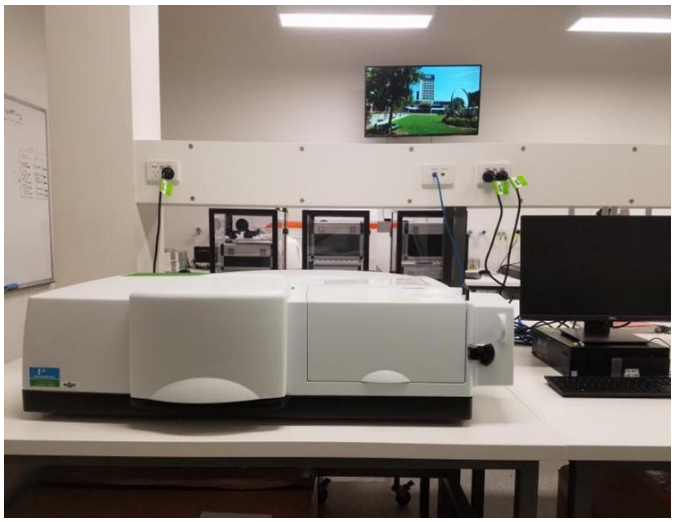

Figure 17. Photo of PerkinElmer | Lambda 1050 | UV/Vis/NIR Spectrophotometer in spectroscopy laboratory.

3.2.3 X-ray Photoelectron Spectroscopy

XPS is a method that uses an electron spectrometer to measure the energy distribution of photoelectrons and Auger electrons emitted from the sample surface when irradiated by X-ray photons. XPS can be used for qualitative analysis and semi-quantitative analysis. Generally, information on the surface element composition, chemical state and molecular structure of the sample is obtained from the peak position and peak shape of the XPS spectrum, and the content or concentration of the sample surface element can be obtained from the peak intensity. Since electrons need to consume energy through materials, and

their intensity is subject to an exponential decay law, XPS is mainly used for surface analysis, and its information depth is greatly affected by the sample state and X-ray wavelength. Generally, 3 times the photoelectron wavelength, *i.e.* 3λe is defined as the information depth of XPS. The test depth of commonly used inorganic materials is generally around 5-10nm.

The commonly used X-ray source is an Al-Kα ray monochromatic source with an energy of 1486.6 eV, which excites the electron transition of the inner energy level of the atom and escapes from the sample surface because photoelectrons carry the characteristic information of the sample (element information, chemical state information, etc.), the mechanism is illustrated in **Figure 18(a)**. By measuring the kinetic energy of escaped electrons, the elemental composition and chemical state information in the sample will be known, which are obtained from the core equation:

$$E(b) = h\nu - E(k) - \varphi(4)$$

where E(b) is the binding energy, hν is photo energy, E(k) is the kinetic energy of the electron and φ is the spectrometer work function. As shown in **Figure 18(b)**, Thermo ESCALAB250Xi X-ray photoelectron spectrometer is in charge of the XPS measurement in this work.

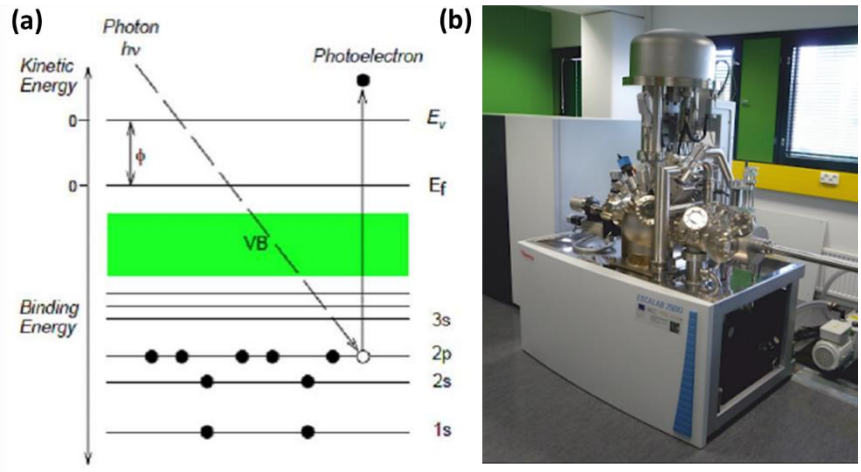

Figure 18. (a) Schematic illustration of the mechanism of XPS (b) Photo of Thermo ESCALAB250Xi X-ray photoelectron spectrometer in Surface Analysis Laboratory

3.2.4 Photoluminescence (PL) measurement

Photoluminescence spectroscopy is used to detect the electronic structure of materials and is a non-contact, non-damaging test method. In principle, light irradiates the sample and is absorbed by the sample, resulting in a light excitation process. Light excitation causes the material to transition to a higher electronic state, then release energy after the relaxation process, and (photons) return to a lower energy level. The light radiation or luminescence in this process is called photoluminescence (PL). The bandgap of the semiconductor material could be calculated through the PL peak position, which could identify the composition of the material. Moreover, identification of impurity, the luminous efficiency of materials, lifetime of the charge carrier in semiconductor could obtain from PL spectroscopy as well. PL spectra are obtained by WiTech Alpha300 confocal Raman spectroscopy (**Figure 19**) with 532nm lasers.

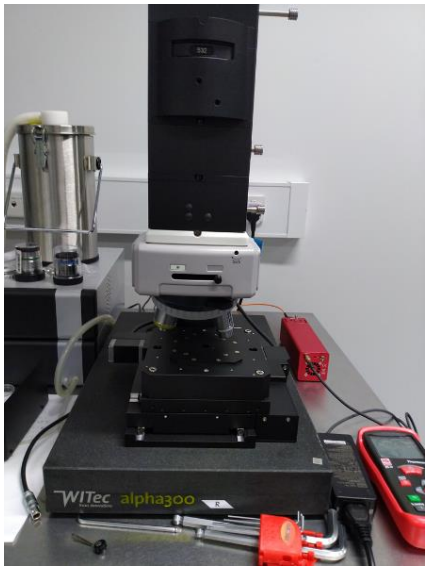

Figure 19. Image of WiTech Alpha300 confocal Raman spectroscopy used in this work.

3.3 Electrical properties of Ag-Doped Single Crystal

In addition to basic characterizations of Ag-doped single crystal, electrical properties are also investigated in this project. Carrier concentration and mobility of the sample are measured by Hall effect measurement. Moreover, the mobility of Ag-doped single crystals is calculated from Space-charge limited current method as well to compare with the result of hall effect measurement. Two methods used will be introduced below.

3.3.1 Space-Charge-Limited-Current (SCLC) Method

Space-charge-limited-current (SCLC) method has been used intensively to obtain mobility of HOIP materials in recent years[15,59,84,88,94,96], which the relationship between the current betwixt two electrodes on the sample and the applied bias voltage is the core of this method. Three different regions are shown in the I-V curve of the semiconductor with bias voltage increased, which are Ohmic region, Trap-filled limited (TFL) region and Child region, respectively. At low voltage region, currents are dominated by the thermally generated charge carriers, exhibiting ohmic contact behavior in the Ohmic region, which the current is linear with a bias voltage ($J \propto V$). As voltage rises, excess

injected charge carriers are trapped by the traps in semiconductor material, resulting the TFL region. When the voltage has been excess V_{TFL}, traps in semiconductors are filled with injected carriers which means other injected carriers can effortlessly without restraint, which the current is linear with the square of bias voltage ($J \propto V^2$). When the trap-free region is reached, mobility of charge carrier can be derived from the Mott-Gurney's law[97]:

$$J_D = \frac{9\varepsilon\varepsilon_0\mu {V_b}^2}{8L^3} (5)$$

where ε and ε_0 are relative dielectric constant and vacuum permittivity, respectively. J_D is current density, V_b is a voltage selected from the Child region, L is the thickness of samples. Furthermore, the trap-state density of material can be known by SCLC method as well, which onset voltage(V_{TFL}) in TFL region is critical for the equation:

$$N_{traps} = \frac{2\varepsilon\varepsilon_0 V_{TFL}}{qd^2} (6)$$

where ε=25.5[88] for $MAPbBr_3$, q is the charge of electron and d is the thickness of the sample.

To get information from the I-V curve more intuitively, logarithm is applied on current and voltage on the graph, which the X-axis is Log V and the Y-axis is Log I. Log I – Log V curve is divided into three part with various slope, which the slope of Child region is twice as high as the slope of the Ohmic region. The value of voltage used in Mott-Gurney's law is crucial for the value of mobility, thus, several voltages will be selected for the calculation and the result of mobility will be the average value. To fabricate the device for SCLC measurement, Au electrodes are deposited on the surfaces of the single crystal by the evaporator, which the thickness of the Au electrodes is around 100 nm. The structure of SCLC measurement device is shown in **Figure 20(a)**, electrodes are

distributed in the four corners of the two largest faces of the cuboid. To minimize the error, two probes of the probe station are contacted with two electrodes located at the same corner, and each corner will be measured. I-V curve is analyzed by Keithley 4200 (**Figure 20(c)**) which connect with the probe station. Single crystal with Au electrode, probe station with two probes and the evaporator used for electrodes deposition are shown in **Figure 20(b) (d) (e)**.

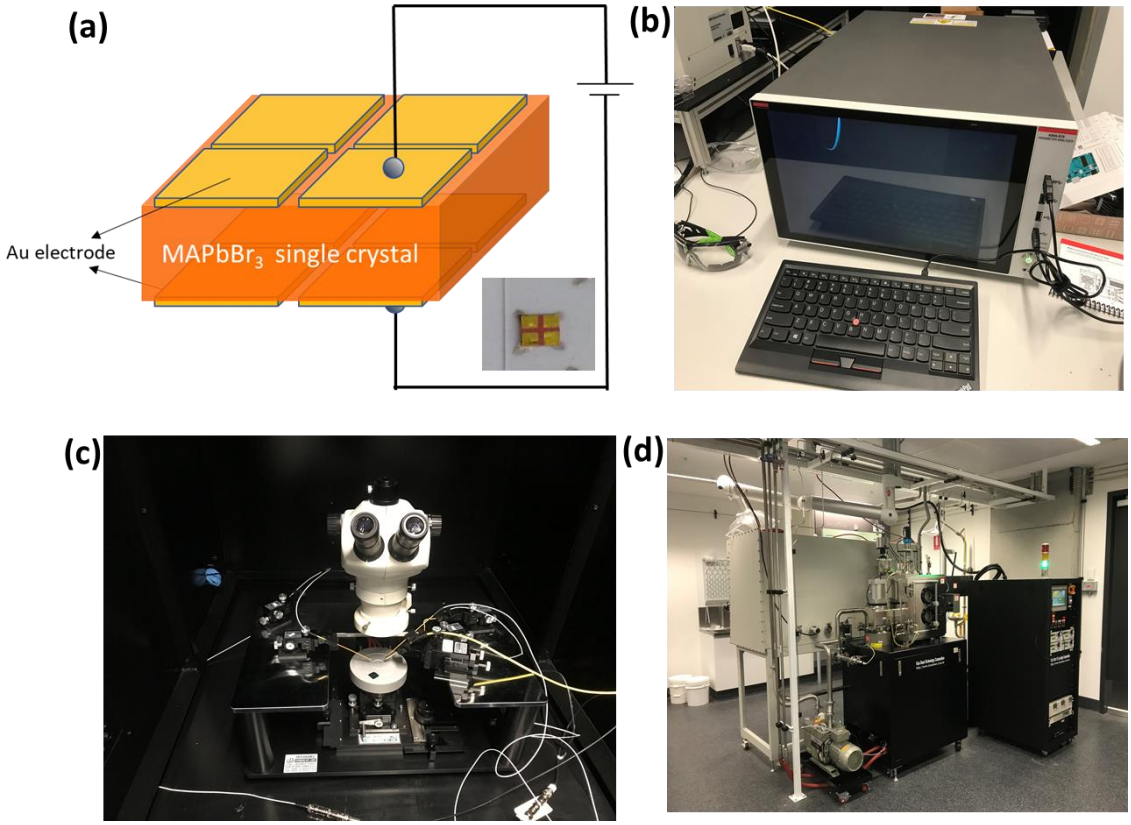

Figure 20. (a) Structure of sinlge crystal device for SCLC measurement. Inset is the photo of electrodes deposited Ag-doped $MAPbBr_3$ sinlge crystal (b) Probe station used for contacting with samples (c) Keithley 4200A-SCS Parameter connected with probe station for analyzing data. (d) Evaporator used for Au electrodes deposition in this project.

3.3.2 Hall Effect Measurement

Through Hall effect measurement, the carrier concentration, type (N-type or P-type),

conductivity and mobility of semiconductor materials can be calculated. The current-carrying sample is placed in a magnetic field with a magnetic induction strength of B. An electrical field perpendicular to the direction of the current and magnetic induction is generated at both ends of the sample perpendicular to the current and magnetic field, which called Hall effect. Through the direction of the electrical field, the Hall effect can directly distinguish the type of the majority carrier, which are electrons or holes. Moreover, Hall resistivity (ρ_H) can be calculated from the equation:

$$\rho_H = \frac{RLT}{W} (7)$$

where R is Hall resistance and L, T, W are the dimensions of the sample. Hall coefficient (R_H) is critical for calculating other parameters *i.e.* charge carrier density and mobility measured be hall effect, the equation is followed :

$$R_H = \frac{V_H T}{I_s B} (8)$$

where V_H is the voltage generated by Hall effect and B is the magnetic field. Since Hall coefficient is known, charge carrier density and mobility can be obtained by:

$$n = -\frac{1}{R_H e} (8)$$

$$\mu = R_H \sigma (9)$$

where e is the charge of electron and σ is the conductivity of the sample.

Figure 21. Physical property measurement system (PPMS) used for Hall effect measurement in this work.

Chapter 4 – Experimental Results and Discussion

4.1 XRD Patterns of Ag-Doped Perovskite Single Crystal

As we can see from **Figure 15**, the color of the Ag-doped $MAPbBr_3$ single crystal gradually changes from orange to dark red as doping level increased, indicating variation has occurred in the crystal structure. Thus, XRD measurement is employed to investigate the difference in crystal structure between undoped and various doping level single crystals. Powder XRD patterns of pure and Ag-doped $MAPbBr_3$ single crystals are shown in **Figure 22(a)**. Compared with the undoped sample, no extra peaks were observed in silver doping samples, indicating that there is no significant change in crystal structure, which keeps cubic structure assigned by $Pm\bar{3}m$ space group.

However, as shown in **Figure 22(b)**, the peak position of (100) face exhibits left shift, which the diffraction angle corresponding to (100) face becoming smaller as doping concentration increases. According to Bragg's Law, the reduction of the variation θ, resulting in the increment on the lattice parameter of crystal structure. To be more specific, the lattice parameter of sliver doped samples is increased from 5.88 Å for the pristine single crystal to 5.93 Å with 5% silver doping level single crystal. Surprisingly, the expansion trend of the lattice parameter is not monotonously, in which the 10% doped sample shows a 0.01 Å shorter than 5% doped sample, suggesting the doping level limit of silver ions in $MAPbBr_3$ is less than 10%. (**Figure 22(d)**) The same conclusion is

obtained from UV-Vis results again. Furthermore, the diffraction angle of (200) face shows decreasing tendency, confirming the lattice expansion occurred on Ag-doped crystal structure. Since the radius of silver ions is 126 pm,[98] which 7 pm longer than that of lead ions. Thus, lattice expansion could be explained by the partial substitution of lead ions by silver ions. However, if the replaced site of $MAPbBr_3$ is A-site, which the radius of MA^+ ions is 216 pm[99], lattice parameter will be decreased instead of increasing, indicating Ag ions will more likely to substitute lead ions in $MAPbBr_3$. Moreover, as we discussed above, perovskite structure can be formed when the tolerance factor is between 0.8~1. Compared with large MA^+ cation, silver ions have a more similar size with lead ions in the B-site, which would not cause too much distortion on the lattice. Tolerance factor of silver on B-site is between that range but that of silver on A-site is less than 0.8, which could not form a stable perovskite structure, suggesting silver ions doping is more likely a B-site doping work as well.

In addition to variation on lattice parameter was observed from powder XRD pattern, the intensity of each peak is also displayed on the graph. As shown in **Figure 22 (a)**, 1% Ag doping sample possesses two sharpest peaks, which are (200) and (221) faces, indicating the good quality of Ag-doped single crystals. Crystallinity enhancement by Ag doping has been proved by two works of Chen et al.[50] and Zhou et al.[51] recently, which the conclusion is consistent with our result. To sum up, lattice expansion on Ag-doped single crystal and quality-enhanced Ag-doped single crystals are confirmed by powder XRD pattern of samples.

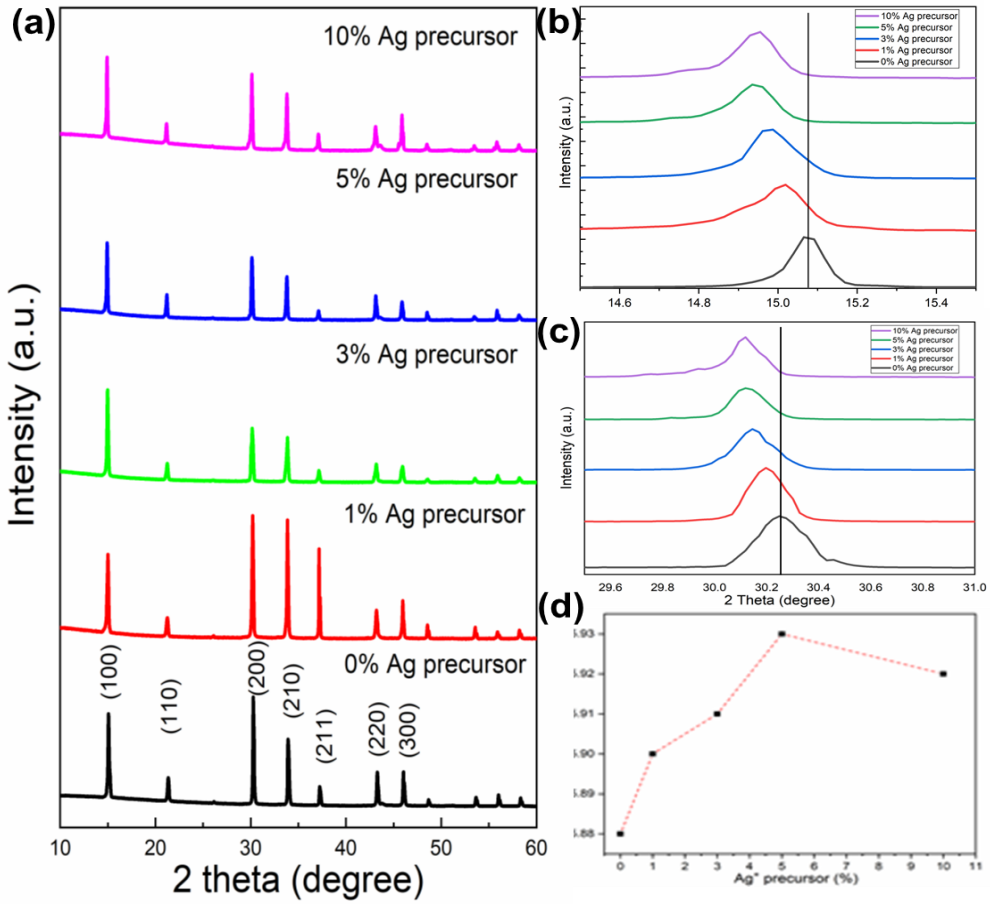

Figure 22. (a) Powder XRD pattern of undoped and Ag-doped $MAPbBr_3$ single crystal with various doping levels. (b)(c) Magnified view of (100) XRD peak and (200) XRD peak in each sample, respectively. (d) d-spacing of (100) planes of each sample against Ag doping level.

Single crystal pattern XRD was also employed in this project, however, only the crystal structure and lattice parameter can be determined by the machine. The results of single crystal pattern XRD indicate the crystal structure of the Ag-doped single crystal is same as that of undoped sample, which is a cubic structure. Lattice parameters of undoped single crystal and Ag-doped single crystal are slightly longer than calculated result from powder pattern, which the results for undoped and 5% doping samples are 5.90 Å and 5.95 Å. The difference between the two patterns may be caused by the different precision of two instruments.

4.2 XPS Results of Ag-Doped Perovskite Single Crystal

To investigate the element composition of $MAPb_xAg_{1-x}Br_3$ single crystal, we employed XPS to detect the surface of the samples with around 5-10 nm depth. Newly cleaved surfaces of $MAPb_{1-x}Ag_xBr_3$ single crystals with five X value (0, 1, 3, 5, 10) are placed into an XPS chamber, XPS spectra of each sample are shown in **Figure 23(a)**. The core layers of $MAPbBr_3$ are marked in spectra, which are Br 3d Br 3p Br 3s, Pb $4f_{7/2}$ Pb $4f_{5/2}$, C 1s and N 1s. The binding energy of Pb $4f_{7/2}$, Pb $4f_{5/2}$, and Br 3d is 139.2 eV, 144.3 eV and 68.9 eV, respectively, which are slightly higher than the reported results of $MAPbBr_3$ polycrystalline thin film,[100] suggesting the impact of different chemical environment. Peaks of C 1s and N 1s are located at 286.4 eV and 402.3 eV, which are consistent with value of Bi-doped $MAPbBr_3$ single crystal.[74] Higher binding energy of each peak of this sample than thin films may be caused by the worse crystal conduction between bulk and XPS instrument.

Furthermore, other evidence demonstrates the success of Ag doping into $MAPbBr_3$ single crystal is provided by the XPS spectra of Ag 3d. XPS spectra of samples with various doping levels are shown in **Figure 23(b)**. As expected, no peak in the Ag 3d region was observed for pristine single crystal. However, two peaks affiliated with Ag $3d_{5/2}$ and $3d_{3/2}$ at 368 eV and 374 eV, respectively, start to appear after the incorporation of silver. Moreover, intensities of two peaks are enhanced after Ag doping level increasing from 1% to 10%, demonstrating the successful work of Ag doping work and the controllable Ag

concentration in $MAPbBr_3$ single crystals.

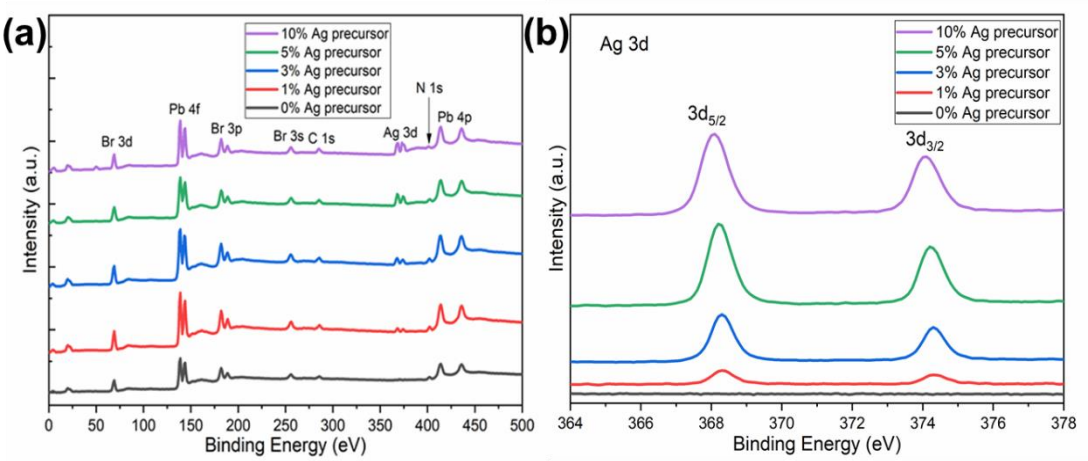

Figure 23. (a) Full XPS spectra and (b) Ag 3d region of $MAPb_xAg_{1-x}Br_3$ single crystal with various X value (0, 1, 3, 5, 10).

4.3 Optical Properties of Ag-Doped Perovskite Single Crystal

4.3.1 Photoluminescence Spectra of Ag-Doped Perovskite Single Crystal

PL spectra of Ag doped $MAPbBr_3$ single crystals are displayed in **Figure 24(a)**. The pristine single crystal exhibits an emission peak at 538 nm, in which the calculated bandgap is larger than the value obtained from the Uv-Vis absorption measurement.[101] A possible explanation for the difference between emission peak and absorption peak is the Anti-Stokes shift, in which the position of the emission peak is to the left of the position of the absorption peak.

Significant PL quenching can be observed in **Figure 24(a)**, as Ag doping level increases, the intensity of emission peaks are dropped monotonously, which the behavior is consistent with Ag doped hybrid halide perovskite thin films. PL quenching of Ag doped perovskite single crystal is caused by the efficient charge transfer between silver ions and $MAPbBr_3$. The small emission peaks at 532nm in each sample are from the laser used in

the PL instrument.

Moreover, emission peaks of each sample exhibit slightly redshift as doping level increases, which the tendency is consistent with the result of absorption measurement. The redshift occurs on the PL peak suggests that the bandgap of Ag-doped single crystals is reduced, however, because the surface of the bulk sample is not smooth enough and accompanied by defects, only slightly redshift can be observed from **Figure 24 (b)**. It indicates that efficient charge transfer between host and Ag occurs and the bandgap of samples is narrowed due to the inclusion of silver ions.

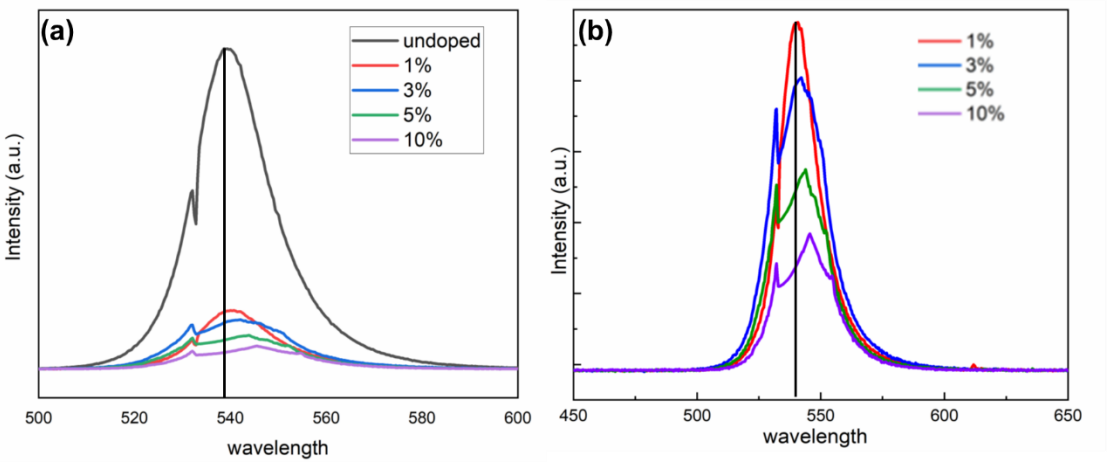

Figure 24. (a) PL spectra of $MAPb_xAg_{1-x}Br_3$ single crystal with various X value (0, 1, 3, 5, 10). (b) Magnified view of (a) without undoped sample.

4.3.2 Optical Absorption Spectra of Ag-Doped Perovskite Single Crystal

UV-Vis absorption measurement was applied to $MAPb_xAg_{1-x}Br_3$ single crystal to obtain the bandgap of each sample. Tauc plots correspond to the absorption spectra of each sample are shown in **Figure 25**, after normalizing area and thickness of samples. It is shown that the optical bandgap of Ag doped $MAPbBr_3$ single crystal is narrowed from 2.21 eV to 2.05 eV as sliver doping concentration rises from 0% to 5%. However, no further bandgap narrowing is exhibited when silver doping level reached 10%, suggesting

the doping limitation of sliver ions in perovskites may be exceeded, which is consistent with the XRD results and surface quality of 10% Ag-doped single crystal. The reduction bandgap of doped samples induced by the interaction between the electrons and positive dopants, adjusting the density of states.[102] Conduction band and valence band of perovskites are determined by the outer orbitals of B-site and X-site elements, thus, optical property such as bandgap could be affected by B-site doping, which could explain the reduction tendency of Ag doped samples as well.

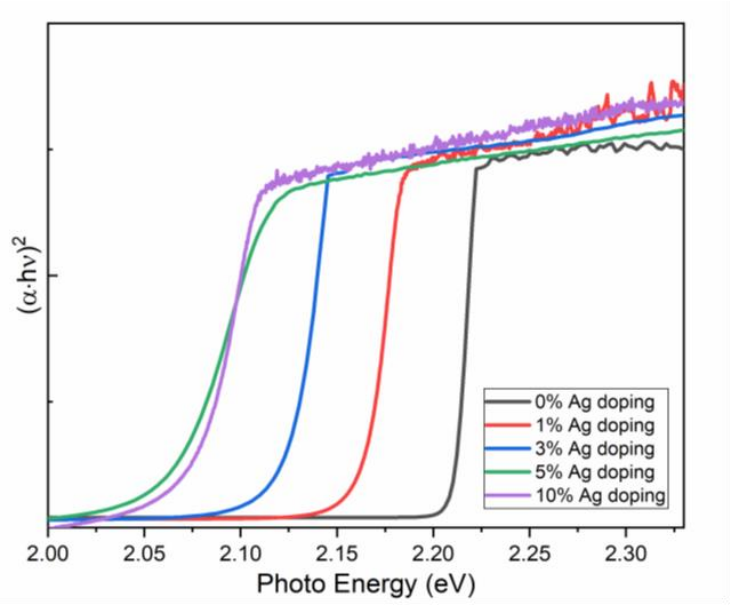

Figure 25. Tuac plots corresponding to absorption spectra of Ag doped samples with various doping concentrations.

4.4 Electrical Properties of Ag-Doped Perovskite Single Crystal

The electrical properties of materials play a decisive role in the development of their applications. Therefore, SCLC measurement and Hall effect measurement are adopted in this project to measure the conductivity and mobility of Ag-doped $MAPbBr_3$ single crystals. The results are discussed below.

4.4.1 Hall Effect Results

Ag-doped samples were ground to 1mm thickness to meet the sample requirement of PPMS equipment, and four silver electrodes are distributed at four corners of the top surface of the sample. As expected, the majority charge carrier type is confirmed as holes, and the type of $MAPbBr_3$ is converted from intrinsic to P-type semiconductor. Moreover, the carrier concentration of undoped and Ag-doped samples is examined as well, in which the concentration increases from $4.38 * 10^{10}$ cm^{-3} for the intrinsic sample to $5.26 * 10^{10}$ cm^{-3} for 3% Ag doped sample at 280K, indicating only small part of dopants can contribute free carriers.

As displayed in **Figure 26(a)**, the resistance of the pristine $MAPbBr_3$ single crystal increases from 127 MΩ to 1859 MΩ when the temperature decreases from 320 K to 220 K. Taken into account the sample dimension and measurement configuration, the same temperature (320K) resistivity of the undoped single crystal is approximately 279 MΩ cm. After doping 3% Ag ions, the room-temperature resistance decreased by almost four times. The resistance of the doped single crystal shows a similar trend like the undoped one with its resistance increasing to 917 MΩ cm when the temperature decreases to 220 K. Overall, the Ag-doped MAPbBr3 single crystal is much more conducting than the undoped counterpart, which is consistent with the enhanced mobility revealed by the SCLC measurement and Hall effect measurement.

In addition to carrier concentration and conductivity, mobility of Ag-doped samples is also measured by Hall effect, in which the mobility of undoped sample and 3% Ag doped sample are 18.9 cm^2/Vs and 65.7 cm^2/Vs, respectively. Since the conductivity of semiconductors is related to its carrier concentration and mobility,[103] the product of the respective growth multiples of carrier concentration and mobility should be equal to the growth multiple of conductivity. According to the results, the product of two parameters is 3.99 which is consistent with the multiple conductivity.

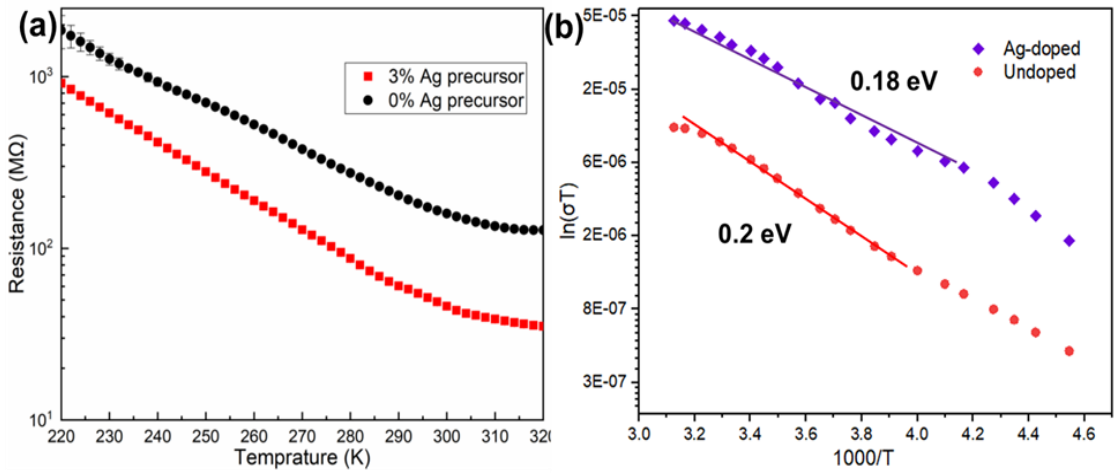

Figure 26. (a) Temperature-dependent resistance of undoped and Ag-doped $MAPbBr_3$ single crystals. (b) Conductivity against T^{-1} in log scale for Ag-doped and undoped $MAPbBr_3$ single crystal, respectively.

To understand the carrier transport in $MAPbBr_3$ single crystal, we further researched the temperature dependence of the conductivity. As shown in **Figure 26(b)**, the ion activation energy (E_A) in the 220K-320K temperature region is obtained by using the Nernst-Einstein relation:

$$\sigma(T) = \frac{\sigma_0}{T} \exp\ (-E_A/K_B T) (10)$$

in which σ_0 is a constant, K_B and T are the Boltzmann constant and temperature,

respectively.[104] The activation energy (E_A) could be obtained from the slope of the ln σ(T) and 1/T relation. For undoped single crystal, the activation energy at 220K-320K is 0.2 eV which is 0.02 eV higher than that of Ag-doped single crystal. The small E_A value demonstrates that thermally activated transport is caused by the defect level. Since E_A represents the depth from CB to defect level, indicating that the defect level of Ag-doped sample is shallower than the undoped one, which benefits the charge transport in semiconductor. As concluded by Hall effect measurement, type of majority charge carrier in samples is hole, along with carrier concentration, conductivity and mobility of samples are raised with the incorporation of silver ions.

4.4.2 Space-Charge-Limited-Current (SCLC) Measurement Results

Mobility is a physical quantity used to describe the moving speed of charge carriers, affecting the development of applications based on semiconductor material. Despite mobility results measured by Hall effect method is displayed above, SCLC method is mainly used to reveal the mobility and trap state density of $MAPb_xAg_{1-x}Br_3$ single crystals. Log I versus Log V curve of each sample are shown in **Figure 27**, mobility of pure $MAPbBr_3$ single crystal is calculated as 42 cm^2/Vs, which is higher than the reported value, signifying better crystal quality in this work. Moreover, as doping concentration rises from 0 to 5%, a gradual upward trend of mobility can be observed, which the value increases from 42±3 cm^2/Vs to 243±16 cm^2/Vs. However, the upward trend is not monotonously in the range of 0-10% doping level, which the mobility is reduced when doping concentration exceeds 5%. It is also consistent with the results of XRD and optical absorption. Opposite with the upward trend of mobility, trap state density of samples

exhibits a dropping tendency as Ag doping level increases. The trap state density 5% Ag doped sample is (4.2±0.6)*10^9 cm^{-3}, which is 43% lower than the pure sample, suggesting shallow acceptor levels are created by silver ions.

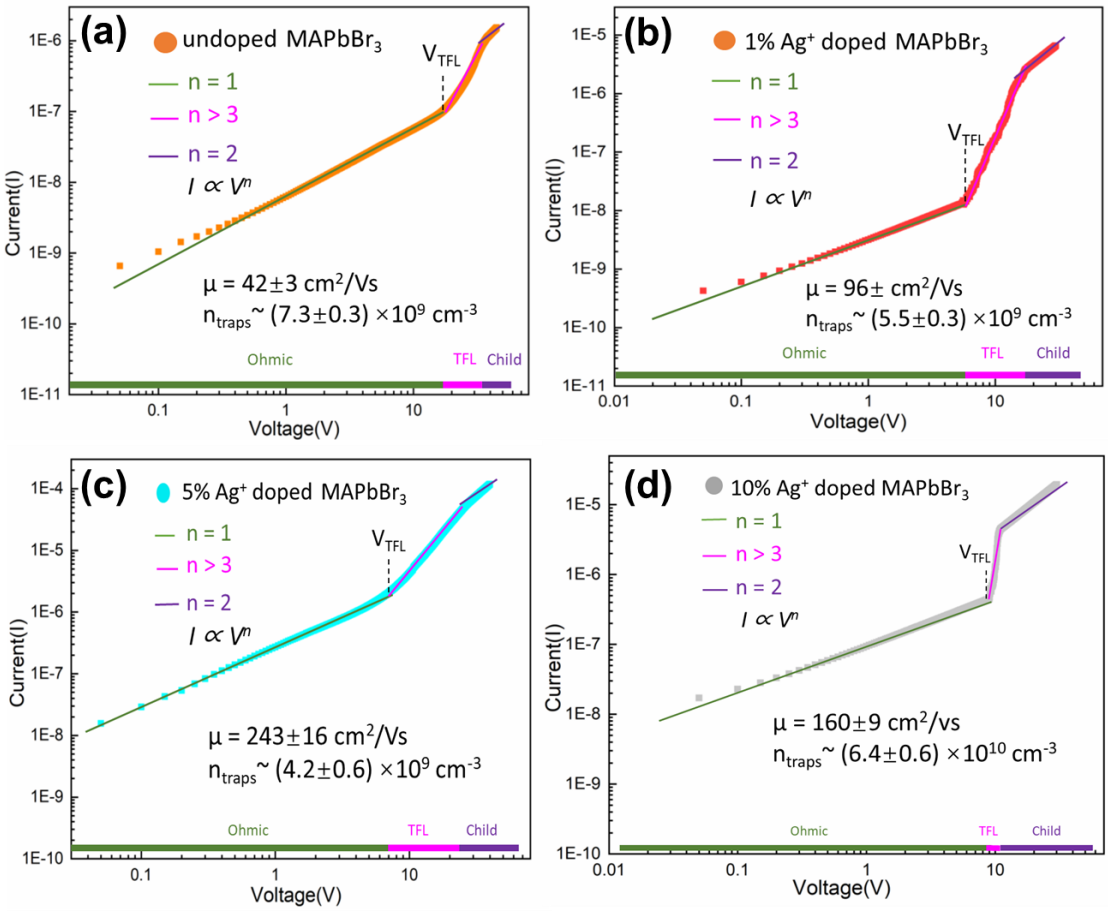

Figure 27. Current-voltage traces and trap density for (a) 0%, (b) 3%, (c) 5%, and (d) 10% Ag^+ doped $MAPbBr_3$ single crystals. As applied voltage increases, the linear Ohmic region transits to trap-filled region, illustrated by a dramatic rise in current, and finally falls into the trap-free child's region at high voltage.

The discrepancy of mobility value between Hall effect and SCLC can be elucidated by the ion migration occurred inside the perovskite.[105] Besides that, the thickness of the sample is also a tricky issue in Hall effect measurement, damages and defects are created on crystals after grinding, affecting the result of mobility.

To explain the enhancement of mobility of Ag-doped $MAPbBr_3$ single crystals, Frohlich interaction should be introduced. The charge carrier mobility depends on the effective mass of electrons, in which the value can be affected by the electron-phonon coupling. In halide perovskites, Frohlich coupling plays a very important role in affecting the interaction between electron and lattice crystal vibration.[106] Mobility of the pristine perovskite is limited by the heavy metal attributes to Frohlich interaction. Therefore, by substituting Pb with lighter element Ag, the Frohlich interaction can be suppressed, leading to the reduced effective mass of electrons as well as the higher mobility as observed in the Ag-doped perovskite.

4.5 Photodetector Performance Based on Ag-Doped Perovskite Single Crystal

After revealing the optoelectronic properties of Ag-dopes $MAPbBr_3$ single crystal, photodetector based on this modified material was fabricated. Similar to the device structure for SCLC measurement, Au electrodes with mask shapes are deposited on the top surface of the sample. As shown in **Figure 28**, current-voltage traces of the photodetector based pure and 5% Ag-doped samples were measured in the dark and light condition under light illumination of the 450nm light source. The dark current and photocurrent of Ag-doped photodetector are $5.08 * 10^{-6}$ A and $1.4 * 10^{-5}$ A at 10V. The high dark current can be explained by the introduction of silver ions inside the crystal, which makes the material more conductive. Responsivity (R) can be calculated from the equation[107,108]:

$$R = \frac{I_L - I_D}{P_L * S} (11)$$

in which I_L and I_D represent photocurrent and dark current, P_L is the light intensity of light

source and S is the active area.

As expected, compared with regular photodetector, the responsivity of Ag-doped photodetector is increased from 0.72 A W^{-1} to 1.58 A W^{-1} which can attribute to the improved conductivity of Ag-doped sample. However, the result is relatively lower than other reports due to the high dark current and high thickness of samples.

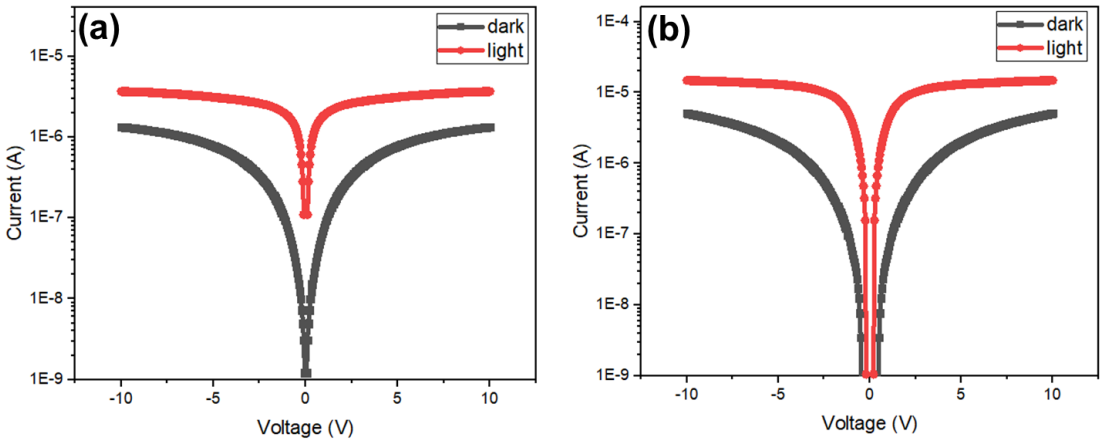

Figure 28. Current (I) include dark current and photocurrent versus voltage (V) curve of photodetectors based on (a) pristine $MAPbBr_3$ single crystal and (b) 5% Ag-doped $MAPbBr_3$ single crystal.

Chapter 5 – General Conclusion and Perspectives

In this work, the modified LTHMC method was employed to synthesize high quality Ag-doped $MAPbBr_3$ single crystals. Half centimeter-size single crystal can be obtained within two days. At first, the structure of Ag-doped single crystals is confirmed by both powder and single crystal XRD patterns. Lattice parameter expansion occurs in the Ag-doped single crystal with various doping levels. Successful Ag-doping work is demonstrated by XPS, which is consistent with the XRD result.

After that, tunable bandgap of $MAPb_xAg_{1-x}Br_3$ single crystal is validated by UV-Vis absorption tests, which it drops from 2.21eV to 2.05eV after 5% Ag doping level. Moreover, PL quenching was also observed in the PL spectra due to efficient charge transfer between dopants and host.

In addition to optical properties, electrical properties of $MAPb_xAg_{1-x}Br_3$ single crystal were revealed as well. Ag-doped is P-type semiconductor materials were confirmed by Hall effect measurement. Moreover, better conductivity and higher carrier concentration of Ag-doped sample were also proved by Hall effect. Besides that, mobility enhancement was demonstrated by SCLC method. $MAPb_xAg_{1-x}Br_3$ single crystals exhibit higher mobility with a lower trap-state density as Ag doping level increases from to 5%. However, compared with the 5 % Ag-doped sample, 10% Ag-doped sample exhibits lower mobility and higher trap-state density, suggesting the limitation of Ag doping level. In the end, photodetector based on Ag-doped single crystal was fabricated. The responsivity of Ag-doped photodetector is higher than the pure one. However, due to the relatively high dark current and higher thickness of the device, the performance of photodetectors is not as promising as expected, which awaits to be further discussed in the future.

Despite the encouraging progress that has been made on perovskite single crystal applications, there are still some impediments restraining its development, such as high thickness and toxicity of single crystal. Even the longest reported carrier diffusion length of perovskite single crystal (175 micrometers)[84] is not enough for several optoelectronic devices. Thus, single crystal thin film with micrometer-sized with excellent photophysical

properties is expected to draw intensive attention in the future. Furthermore, results from this project have demonstrated that monovalent ions doping such as Ag could be a feasible path to alter the electrical and optoelectronic properties of perovskite single crystal. It is expected that metal doped perovskite single crystal film might trigger a new evolution on optoelectronic devices including PSC, LED, lasers and transistors.

Chapter 6 – Reference

1. Chakhmouradian AR, Woodward PM. Celebrating 175 years of perovskite research: a tribute to Roger H. Mitchell. In: Springer; 2014.
2. Li W, Wang Z, Deschler F, Gao S, Friend RH, Cheetham AKJNRM. Chemically diverse and multifunctional hybrid organic–inorganic perovskites. 2017;2(3):16099.
3. MØLLER CKJN. Crystal structure and photoconductivity of caesium plumbohalides. 1958;182(4647):1436-1436.
4. Weber DJZfNB. CH3NH3PbX3, ein Pb (II)-system mit kubischer perowskitstruktur/CH3NH3PbX3, a Pb (II)-system with cubic perovskite structure. 1978;33(12):1443-1445.
5. Liu M, Johnston MB, Snaith HJJN. Efficient planar heterojunction perovskite solar cells by vapour deposition. 2013;501(7467):395-398.
6. Zhou H, Chen Q, Li G, et al. Interface engineering of highly efficient perovskite solar cells. *Science.* 2014;345(6196):542-546.
7. Eperon GE, Stranks SD, Menelaou C, et al. Formamidinium lead trihalide: a broadly tunable perovskite for efficient planar heterojunction solar cells. 2014;7(3):982-988.
8. Zhu H, Fu Y, Meng F, et al. Lead halide perovskite nanowire lasers with low lasing thresholds and high quality factors. 2015;14(6):636-642.
9. Sutherland BR, Sargent EHJNP. Perovskite photonic sources. 2016;10(5):295.
10. Xing G, Mathews N, Lim SS, et al. Low-temperature solution-processed wavelength-tunable perovskites for lasing. 2014;13(5):476.
11. Lin C-H, Li T-Y, Zhang J, et al. Designed growth and patterning of perovskite nanowires for lasing and wide color gamut phosphors with long-term stability. 2020:104801.
12. Stranks SD, Snaith HJJNn. Metal-halide perovskites for photovoltaic and light-emitting devices. 2015;10(5):391.

13. Cao Y, Wang N, Tian H, et al. Perovskite light-emitting diodes based on spontaneously formed submicrometre-scale structures. 2018;562(7726):249-253.
14. Kang CY, Lin CH, Lin CH, et al. Highly Efficient and Stable White Light-Emitting Diodes Using Perovskite Quantum Dot Paper. 2019;6(24):1902230.
15. Maculan G, Sheikh AD, Abdelhady AL, et al. CH3NH3PbCl3 single crystals: inverse temperature crystallization and visible-blind UV-photodetector. 2015;6(19):3781-3786.
16. Wei H, Fang Y, Mulligan P, et al. Sensitive X-ray detectors made of methylammonium lead tribromide perovskite single crystals. 2016;10(5):333.
17. Fang Y, Dong Q, Shao Y, Yuan Y, Huang JJNP. Highly narrowband perovskite single-crystal photodetectors enabled by surface-charge recombination. 2015;9(10):679.
18. Saidaminov MI, Haque MA, Almutlaq J, et al. Inorganic lead halide perovskite single crystals: phase-selective low-temperature growth, carrier transport properties, and self-powered photodetection. 2017;5(2):1600704.
19. Yu W, Li F, Yu L, et al. Single crystal hybrid perovskite field-effect transistors. 2018;9(1):1-10.
20. Choi J, Han JS, Hong K, Kim SY, Jang HWJAM. Organic–inorganic hybrid halide perovskites for memories, transistors, and artificial synapses. 2018;30(42):1704002.
21. Liu X, Yu D, Song X, Zeng H. Metal Halide Perovskites: Synthesis, Ion Migration, and Application in Field-Effect Transistors. In. Vol 142018:n/a-n/a.
22. Guan X, Wang Z, Hota MK, Alshareef HN, Wu TJAEM. P-Type SnO Thin Film Phototransistor with Perovskite-Mediated Photogating. 2019;5(1):1800538.
23. Guan X, Hu W, Haque MA, et al. Light-responsive ion-redistribution-induced resistive switching in hybrid perovskite Schottky junctions. 2018;28(3):1704665.
24. Yoo EJ, Lyu M, Yun JH, Kang CJ, Choi YJ, Wang LJAM. Resistive switching behavior in organic–inorganic hybrid CH3NH3PbI3− xClx perovskite for resistive random access memory devices. 2015;27(40):6170-6175.

25. Shan Y, Lyu Z, Guan X, et al. Solution-processed resistive switching memory devices based on hybrid organic–inorganic materials and composites. 2018;20(37):23837-23846.
26. Ge S, Guan X, Wang Y, et al. Low-Dimensional Lead-Free Inorganic Perovskites for Resistive Switching with Ultralow Bias. 2020:2002110.
27. Berry J, Buonassisi T, Egger DA, et al. Hybrid Organic–Inorganic Perovskites (HOIPs): Opportunities and Challenges. *Advanced Materials.* 2015;27(35):5102-5112.
28. Chen Q, De Marco N, Yang Y, et al. Under the spotlight: The organic-inorganic hybrid halide perovskite for optoelectronic applications. *Nano Today.* 2015;10(3):355-396.
29. Zheng K, Zhu Q, Abdellah M, et al. Exciton binding energy and the nature of emissive states in organometal halide perovskites. 2015;6(15):2969-2975.
30. Kim H-S, Lee C-R, Im J-H, et al. Lead iodide perovskite sensitized all-solid-state submicron thin film mesoscopic solar cell with efficiency exceeding 9%. 2012;2:591.
31. Chen S, Shi GJAM. Two-Dimensional Materials for Halide Perovskite-Based Optoelectronic Devices. 2017;29(24):1605448.
32. Zhao D, Sexton M, Park HY, Baure G, Nino JC, So FJAEM. High-efficiency solution-processed planar perovskite solar cells with a polymer hole transport layer. 2015;5(6):1401855.
33. Yang G, Tao H, Qin P, Ke W, Fang GJJoMCA. Recent progress in electron transport layers for efficient perovskite solar cells. 2016;4(11):3970-3990.
34. Kulbak M, Gupta S, Kedem N, et al. Cesium Enhances Long-Term Stability of Lead Bromide Perovskite-Based Solar Cells. *J Phys Chem Lett.* 2016;7(1):167-172.
35. Mei A, Li X, Liu L, et al. A hole-conductor–free, fully printable mesoscopic perovskite solar cell with high stability. 2014;345(6194):295-298.
36. Berhe TA, Su W-N, Chen C-H, et al. Organometal halide perovskite solar cells: degradation and stability. 2016;9(2):323-356.

37. Kojima A, Teshima K, Shirai Y, Miyasaka TJJotACS. Organometal halide perovskites as visible-light sensitizers for photovoltaic cells. 2009;131(17):6050-6051.
38. Best Research-Cell Efficiency Chart. *https://wwwnrelgov/pv/cell-efficiencyhtml*. 2019.
39. Saparov B, Mitzi D. Organic-Inorganic Perovskites: Structural Versatility for Functional Materials Design. *Chem Rev.* 2016;116(7):4558-4596.
40. Galkowski K, Mitioglu A, Miyata A, et al. Determination of the exciton binding energy and effective masses for methylammonium and formamidinium lead tri-halide perovskite semiconductors. *Energy Environ Sci.* 2016;9(3):962-970.
41. Mitzi DBJJotCS, Dalton Transactions. Templating and structural engineering in organic–inorganic perovskites. 2001(1):1-12.
42. Ono LK, Juarez-Perez EJ, Qi YJAam, interfaces. Progress on perovskite materials and solar cells with mixed cations and halide anions. 2017;9(36):30197-30246.
43. Colella S, Mosconi E, Fedeli P, et al. MAPbI3-xCl x mixed halide perovskite for hybrid solar cells: the role of chloride as dopant on the transport and structural properties. 2013;25(22):4613-4618.
44. McMeekin DP, Sadoughi G, Rehman W, et al. A mixed-cation lead mixed-halide perovskite absorber for tandem solar cells. 2016;351(6269):151-155.
45. Bi D, Tress W, Dar MI, et al. Efficient luminescent solar cells based on tailored mixed-cation perovskites. 2016;2(1):e1501170.
46. Hao F, Stoumpos CC, Chang RP, Kanatzidis MGJJotACS. Anomalous band gap behavior in mixed Sn and Pb perovskites enables broadening of absorption spectrum in solar cells. 2014;136(22):8094-8099.
47. Tang Z, Bessho T, Awai F, et al. Hysteresis-free perovskite solar cells made of potassium-doped organometal halide perovskite. 2017;7(1):1-7.
48. Duong T, Wu Y, Shen H, et al. Rubidium Multication Perovskite with Optimized Bandgap for Perovskite-Silicon Tandem with over 26% Efficiency. *Adv Energy Mater.* 2017;7(14).
49. Choi H, Jeong J, Kim H-B, et al. Cesium-doped methylammonium lead iodide

perovskite light absorber for hybrid solar cells. 2014;7:80-85.

50. Chen Q, Chen L, Ye F, et al. Ag-incorporated organic–inorganic perovskite films and planar heterojunction solar cells. 2017;17(5):3231-3237.

51. Zhou S, Ma Y, Zhou G, et al. Ag-doped halide perovskite nanocrystals for tunable band structure and efficient charge transport. 2019;4(2):534-541.

52. Protesescu L, Yakunin S, Bodnarchuk MI, et al. Nanocrystals of cesium lead halide perovskites (CsPbX3, X= Cl, Br, and I): novel optoelectronic materials showing bright emission with wide color gamut. 2015;15(6):3692-3696.

53. Ogomi Y, Morita A, Tsukamoto S, et al. CH3NH3Sn x Pb (1–x) I3 Perovskite solar cells covering up to 1060 nm. 2014;5(6):1004-1011.

54. Stoumpos CC, Malliakas CD, Kanatzidis MG. Semiconducting tin and lead iodide perovskites with organic cations: phase transitions, high mobilities, and near-infrared photoluminescent properties. *Inorganic chemistry.* 2013;52(15):9019.

55. Zhang X, Cao W, Wang W, et al. Efficient light-emitting diodes based on green perovskite nanocrystals with mixed-metal cations. 2016;30:511-516.

56. Van der Stam W, Geuchies JJ, Altantzis T, et al. Highly Emissive Divalent-Ion-Doped Colloidal CsPb1–x M x Br3 Perovskite Nanocrystals through Cation Exchange. 2017;139(11):4087-4097.

57. Ju D, Dang Y, Zhu Z, et al. Tunable Band Gap and Long Carrier Recombination Lifetime of Stable Mixed CH3NH3Pb x Sn1–x Br3 Single Crystals. 2018;30(5):1556-1565.

58. Lian Z, Yan Q, Gao T, et al. Perovskite CH3NH3PbI3 (Cl) single crystals: rapid solution growth, unparalleled crystalline quality, and low trap density toward 108 cm–3. 2016;138(30):9409-9412.

59. Shi D, Adinolfi V, Comin R, et al. Low trap-state density and long carrier diffusion in organolead trihalide perovskite single crystals. *Science.* 2015;347(6221):519-522.

60. Huang Y, Li L, Liu Z, et al. The intrinsic properties of FA (1− x) MA x PbI 3 perovskite single crystals. 2017;5(18):8537-8544.

61. Han Q, Bae SH, Sun P, et al. Single crystal formamidinium lead iodide (FAPbI3):

insight into the structural, optical, and electrical properties. 2016;28(11):2253-2258.

62. Li W-G, Rao H-S, Chen B-X, Wang X-D, Kuang D-BJJoMCA. A formamidinium–methylammonium lead iodide perovskite single crystal exhibiting exceptional optoelectronic properties and long-term stability. 2017;5(36):19431-19438.

63. Liu W, Lin Q, Li H, et al. Mn2+-doped lead halide perovskite nanocrystals with dual-color emission controlled by halide content. 2016;138(45):14954-14961.

64. Parobek D, Roman BJ, Dong Y, et al. Exciton-to-dopant energy transfer in Mn-doped cesium lead halide perovskite nanocrystals. 2016;16(12):7376-7380.

65. Liu H, Wu Z, Shao J, et al. CsPb x Mn1–x Cl3 Perovskite Quantum Dots with High Mn Substitution Ratio. 2017;11(2):2239-2247.

66. Guria AK, Dutta SK, Adhikari SD, Pradhan NJAEL. Doping Mn2+ in lead halide perovskite nanocrystals: successes and challenges. 2017;2(5):1014-1021.

67. Pérez-del-Rey D, Forgács D, Hutter EM, et al. Strontium Insertion in Methylammonium Lead Iodide: Long Charge Carrier Lifetime and High Fill-Factor Solar Cells. 2016;28(44):9839-9845.

68. Bi Y, Hutter EM, Fang Y, Dong Q, Huang J, Savenije TJJTjopcl. Charge carrier lifetimes exceeding 15 μs in methylammonium lead iodide single crystals. 2016;7(5):923-928.

69. Lau CFJ, Zhang M, Deng X, et al. Strontium-doped low-temperature-processed CsPbI2Br perovskite solar cells. 2017;2(10):2319-2325.

70. Shai X, Zuo L, Sun P, et al. Efficient planar perovskite solar cells using halide Sr-substituted Pb perovskite. 2017;36:213-222.

71. Chan S-H, Wu M-C, Lee K-M, Chen W-C, Lin T-H, Su W-FJJoMCA. Enhancing perovskite solar cell performance and stability by doping barium in methylammonium lead halide. 2017;5(34):18044-18052.

72. Shang M-H, Zhang J, Zhang P, et al. Stable Bandgap-Tunable Hybrid Perovskites with Alloyed Pb–Ba Cations for High-Performance Photovoltaic Applications. 2018;10(1):59-66.

73. Navas J, Sánchez-Coronilla A, Gallardo JJ, et al. New insights into organic–

inorganic hybrid perovskite CH 3 NH 3 PbI 3 nanoparticles. An experimental and theoretical study of doping in Pb 2+ sites with Sn 2+, Sr 2+, Cd 2+ and Ca 2+. 2015;7(14):6216-6229.

74. Abdelhady AL, Saidaminov MI, Murali B, et al. Heterovalent dopant incorporation for bandgap and type engineering of perovskite crystals. 2016;7(2):295-301.

75. Zhou Y, Yong Z-J, Zhang K-C, et al. Ultrabroad photoluminescence and electroluminescence at new wavelengths from doped organometal halide perovskites. 2016;7(14):2735-2741.

76. Begum R, Parida MR, Abdelhady AL, et al. Engineering interfacial charge transfer in CsPbBr3 perovskite nanocrystals by heterovalent doping. 2017;139(2):731-737.

77. Kamat PV, Dimitrijevic NM, Nozik AJTJoPC. Dynamic Burstein-Moss shift in semiconductor colloids. 1989;93(8):2873-2875.

78. Lozhkina OA, Murashkina AA, Shilovskikh VV, et al. Invalidity of band-gap engineering concept for Bi3+ heterovalent doping in CsPbBr3 halide perovskite. 2018;9(18):5408-5411.

79. Smith MD, Karunadasa HIJAocr. White-light emission from layered halide perovskites. 2018;51(3):619-627.

80. Liu M, Zhong G, Yin Y, et al. Aluminum-Doped Cesium Lead Bromide Perovskite Nanocrystals with Stable Blue Photoluminescence Used for Display Backlight. 2017;4(11):1700335.

81. Cheng X, Jing L, Yuan Y, et al. Fe2+/Fe3+ Doped into MAPbCl3 Single Crystal: Impact on Crystal Growth and Optical and Photoelectronic Properties. 2019;123(3):1669-1676.

82. Oku T, Ohishi Y, Suzuki A, Miyazawa YJM. Effects of Cl addition to Sb-doped perovskite-type CH3NH3PbI3 photovoltaic devices. 2016;6(7):147.

83. Wang ZK, Li M, Yang YG, et al. High efficiency Pb–In binary metal perovskite solar cells. 2016;28(31):6695-6703.

84. Dong Q, Fang Y, Shao Y, et al. Electron-hole diffusion lengths > 175 [mu]m in

solution-grown CH3NH3PbI3 single crystals. *Science.* 2015;347(6225):967-970.

85. He Y, Matei L, Jung HJ, et al. High spectral resolution of gamma-rays at room temperature by perovskite CsPbBr 3 single crystals. 2018;9(1):1-8.

86. Poglitsch A, Weber DJTJocp. Dynamic disorder in methylammoniumtrihalogenoplumbates (II) observed by millimeter-wave spectroscopy. 1987;87(11):6373-6378.

87. Dang Y, Liu Y, Sun Y, et al. Bulk crystal growth of hybrid perovskite material CH 3 NH 3 PbI 3. 2015;17(3):665-670.

88. Saidaminov MI, Abdelhady AL, Murali B, et al. High-quality bulk hybrid perovskite single crystals within minutes by inverse temperature crystallization. 2015;6(1):1-6.

89. Liu Y, Zhang Y, Yang Z, et al. Low-temperature-gradient crystallization for multi-inch high-quality perovskite single crystals for record performance photodetectors. 2019;22:67-75.

90. Cheng Z, Liu K, Yang J, et al. High-Performance Planar-Type Ultraviolet Photodetector Based on High-Quality CH3NH3PbCl3 Perovskite Single Crystals. 2019;11(37):34144-34150.

91. Liu Y, Zhang Y, Zhao K, et al. A 1300 mm2 ultrahigh-performance digital imaging assembly using high-quality perovskite single crystals. 2018;30(29):1707314.

92. Liu Y, Yang Z, Cui D, et al. Two-Inch-Sized Perovskite CH3NH3PbX3 (X = Cl, Br, I) Crystals: Growth and Characterization. *Advanced Materials.* 2015;27(35):5176-5183.

93. Lv Q, Lian Z, Li Q, Sun J-L, Yan QJCc. Formic acid: an accelerator and quality promoter for nonseeded growth of CH 3 NH 3 PbI 3 single crystals. 2018;54(9):1049-1052.

94. Zhumekenov AA, Saidaminov M, Haque MA, et al. Formamidinium Lead Halide Perovskite Crystals with Unprecedented Long Carrier Dynamics and Diffusion Length. *ACS Energy Lett.* 2016;1(1):32-37.

95. Tauc J, Grigorovici R, Vancu AJpss. Optical properties and electronic structure of amorphous germanium. 1966;15(2):627-637.

96. Zhumekenov AA, Saidaminov MI, Haque MA, et al. Formamidinium lead halide perovskite crystals with unprecedented long carrier dynamics and diffusion length. 2016;1(1):32-37.
97. Mark P, Helfrich WJJoAP. Space-charge-limited currents in organic crystals. 1962;33(1):205-215.
98. Liu Y, Liu C-y, Rong Q-h, Zhang ZJAss. Characteristics of the silver-doped TiO2 nanoparticles. 2003;220(1-4):7-11.
99. Travis W, Glover ENK, Bronstein H, Scanlon DO, Palgrave RG. On the application of the tolerance factor to inorganic and hybrid halide perovskites: a revised system. *Chem Sci.* 2016;7(7):4548-4556.
100. Kim YH, Cho H, Heo JH, et al. Multicolored organic/inorganic hybrid perovskite light-emitting diodes. 2015;27(7):1248-1254.
101. Kedem N, Brenner TM, Kulbak M, et al. Light-induced increase of electron diffusion length in ap–n junction type CH3NH3PbBr3 perovskite solar cell. 2015;6(13):2469-2476.
102. Palankovski V, Kaiblinger-Grujin G, Selberherr SJMS, B E. Study of dopant-dependent band gap narrowing in compound semiconductor devices. 1999;66(1-3):46-49.
103. Morin F, Maita JPJPR. Conductivity and Hall effect in the intrinsic range of germanium. 1954;94(6):1525.
104. Lin C-H, Li T-Y, Cheng B, et al. Metal contact and carrier transport in single crystalline CH3NH3PbBr3 perovskite. 2018;53:817-827.
105. Duijnstee EA, Ball JM, Le Corre VM, Koster LJA, Snaith HJ, Lim JJAEL. Towards Understanding Space-charge Limited Current Measurements on Metal Halide Perovskites. 2020.
106. Herz LMJAEL. Charge-carrier mobilities in metal halide perovskites: fundamental mechanisms and limits. 2017;2(7):1539-1548.
107. Gong X, Tong M, Xia Y, et al. High-detectivity polymer photodetectors with spectral response from 300 nm to 1450 nm. 2009;325(5948):1665-1667.
108. Periyanagounder D, Wei TC, Li TY, et al. Fast-Response, Highly Air-Stable, and

Water-Resistant Organic Photodetectors Based on a Single-Crystal Pt Complex. 2019:1904634.